AGU ADVANCING EARTH AND SPACE SCIENCE

JGR Earth Surface

RESEARCH ARTICLE

10.1029/2021JF006302

Grounding Line Retreat and Ice Discharge Variability at Two Surging, Ice Shelf-Forming Basins of Flade Isblink Ice Cap, Northern Greenland

Marco Möller[1,2,3], Peter Friedl[4], Steven J. Palmer[5], and Ben Marzeion[1,2]

[1]Institute of Geography, University of Bremen, Bremen, Germany, [2]MARUM – Center for Marine Environmental Sciences, University of Bremen, Bremen, Germany, [3]Geography Department, Humboldt-Universität zu Berlin, Berlin, Germany, [4]Institute of Geography, Friedrich-Alexander-University Erlangen-Nürnberg, Erlangen, Germany, [5]Department of Geography, University of Exeter, Exeter, UK

Key Points:

- After slight advances in the 1996–2001 surges, the grounding lines of basins 2 and 3 retreated 2.2 ± 1.3 km and 2.7 ± 0.9 km until 2019
- Surges of basins 2 and 3 were of "Svalbard-type" whose characteristics were modified by buttressing effects of the downstream ice shelf
- Persistent slowdowns of ice discharge occurred in basins 2 and 3 after the surges, with discharge volumes decreasing by 90% and 96%

Supporting Information:

Supporting Information may be found in the online version of this article.

Correspondence to:

M. Möller,
marco.moeller@uni-bremen.de

Citation:

Möller, M., Friedl, P., Palmer, S. J., & Marzeion, B. (2022). Grounding line retreat and ice discharge variability at two surging, ice shelf-forming basins of Flade Isblink ice cap, northern Greenland. *Journal of Geophysical Research: Earth Surface*, *127*, e2021JF006302. https://doi.org/10.1029/2021JF006302

Received 11 JUN 2021
Accepted 2 FEB 2022

Author Contributions:

Conceptualization: Marco Möller, Ben Marzeion
Formal analysis: Marco Möller, Peter Friedl, Steven J. Palmer
Funding acquisition: Ben Marzeion
Investigation: Marco Möller
Methodology: Marco Möller
Visualization: Marco Möller
Writing – original draft: Marco Möller, Peter Friedl
Writing – review & editing: Marco Möller, Peter Friedl, Steven J. Palmer, Ben Marzeion

Abstract

Ice discharge from Flade Isblink ice cap (NE Greenland) maintains an ice shelf at the northwestern fringe of the ice cap. The two outlet basins feeding this ice shelf surged during the late 1990s. Ice shelves are rare in Greenland and surges of ice shelf terminating glaciers even rarer. Understanding and explaining the evolution of ice mass changes in the two basins is hampered by a lack of knowledge about processes at their grounding zones. We determined, for the first time, the grounding line locations of these basins and analyzed their variability with time. We further quantified ice discharge and its variability during the period 1988–2020. We found that the grounding lines advanced slightly between 1993 and 1999 during the glacier surges, but showed overall retreats of 2.2 ± 1.3 km in basin 2 and 2.7 ± 0.9 km in basin 3 until 2019 over retrograde sloping beds. The retreats were promoted by increasing buoyancy forces due to increasing water depth, but opposing buttressing forces of the ice shelf induced a differing response of the grounding line in the two basins. Based on the observed patterns of flow and retreat, we characterized the surges as "Svalbard-type", modified by buttressing effects of the ice shelf. We calculated total ice discharges over the study period of 1.85 ± 1.59 Gt in basin 2 and 1.38 ± 1.22 Gt in basin 3. We observed reductions in ice discharge of at least 90% after the surges, that persisted for the remainder of the period studied.

Plain Language Summary

The ice cap Flade Isblink (NE Greenland) exhibits a floating ice shelf in front of its northwestern fringe. The two outlet glacier basins which feed this ice shelf experienced surges in the late 1990s. Comparable events have been very rare in Greenland. Little is known about the area where the grounded ice of the two basins of Flade Isblink becomes floating. This hampers an understanding of their ice mass changes. We mapped the grounding lines, that is, the lines where the ice becomes floating, of the two basins at different dates in order to study their variability with time. They advanced slightly together with the surges and afterward retreated by more than 2 km. We also calculated the amount of glacier ice that flowed out of the two basins into the ice shelf over the period 1988–2020: basin 2 lost an ice mass of 1.85 ± 1.59 Gt and basin 3 an ice mass of 1.38 ± 1.22 Gt. After the surges, the ice mass loss per year was at least 90% smaller than during the surges. From our analyses, we concluded that the surges should be characterized as modified "Svalbard-type".

1. Introduction

Ice masses in Greenland showed considerable and increasing mass losses over recent decades (Bevis et al., 2019), contributing significantly to sea level rise and affecting ocean circulation (Rahmstorf et al., 2015; WCRP Global Sea Level Budget Group, 2018). These ice masses comprise the main ice sheet and a total of almost 20,000 surrounding peripheral glaciers (Pfeffer et al., 2014; Rastner et al., 2012). Despite the fact that the combined mass of these peripheral glaciers is only ∼5% of the main ice sheet, they contributed ∼14% to the overall ice mass loss from Greenland in 2003–2008 (Bolch et al., 2013). Over 1961–2016, they contributed ∼3.4 mm to global sea level rise, equaling ∼13% of the global total from glaciers outside the two ice sheets (Zemp et al., 2019). Across northern Greenland in particular, a rapid expansion of ablation areas has led to accelerating ice loss in recent times (Noël et al., 2019). The overall picture of negative surface mass balance of peripheral glaciers in this region (Noël et al., 2017) is supported by observations of widespread ice thinning (Hugonnet et al., 2021).

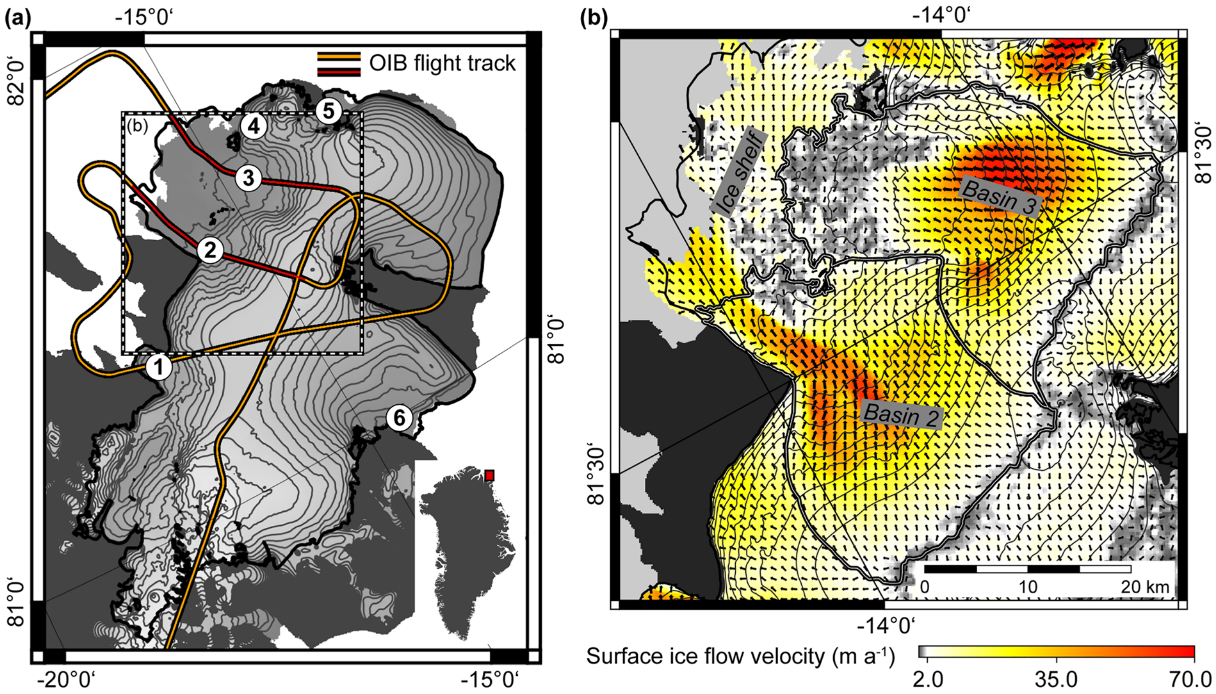

Figure 1. Overview of Flade Isblink ice cap with its location in Greenland (a) and delineation of outlet basins 2 and 3 (b). The light gray (a) and the color (b) grids represent glacierized areas as they are included the MEaSUREs Greenland Ice Mapping Project (GIMP) Land Ice and Ocean Classification Mask V1. The black outline marks the extent of Flade Isblink ice cap according to the RGI 6.0 (Pfeffer et al., 2014). In (a), the circled numbers indicate the six marine-terminating outlet basins of the ice cap, while the colored line shows the course of the Operation IceBridge (OIB) flight track of 6 May 2015. The red parts of this line represent the longitudinal profiles detailed in Figure 5. In (b), the thick black and white outline represents the delineation of basins 2 and 3 that was drawn (cf. Section 3.2) on the basis of 2019 Sentinel-1 surface ice flow velocities (color grid) and directions (arrows). The basin boundaries include the 2018 grounding line (cf. Figure 4f). In both panels, contour spacing on the ice cap is 50 m and dark gray colors indicate glacier-free land areas.

The Flade Isblink ice cap (FIIC) at the northeastern tip of Greenland (Figure 1) represents a clear exception from this general regional behavior. With a surface of ~7,500 km^2 it is the largest of Greenland's peripheral ice masses (Rastner et al., 2012) and one of the largest ice caps in the Arctic (Pfeffer et al., 2014). FIIC is drained by six major marine-terminating outlet basins (Figure 1) (Palmer et al., 2010; Recinos et al., 2021). During 1990–2010, its annual surface mass balances were mostly positive (Rinne et al., 2011). ICESat data suggest that the ice cap experienced an almost zero mass change over 2003–2009 (Bolch et al., 2013; Rinne et al., 2011). FIIC is thus more similar to those large Arctic ice caps that also experienced balanced or slightly positive surface mass balances in recent times (e.g., Moholdt et al., 2012; Möller et al., 2013; Möller & Kohler, 2018; Shepherd et al., 2007) than it is to neighboring glacierized areas in Greenland. The surface mass balance across comparable elevations at the nearby northeastern margin of the Greenland ice sheet was clearly negative (<-0.15 m w. e. a^{-1}) over recent decades (Noël et al., 2016).

Satellite observations of FIIC during 2004–2008 showed an increase in ice thickness over this period resulting from changes in surface geometry (Rinne et al., 2011): integrated over the entire ice cap, a general thinning across the ablation areas was counteracted by a thickening of the accumulation areas. Comparable patterns of ice thickness changes were also observed at ice caps in other regions of the world and were found to indicate intense snowfall in combination with rising air temperatures (Möller & Schneider, 2010). However, at FIIC this general pattern is superimposed by a characteristic NW-SE gradient. Krabill et al. (2000) showed that areas northwest of the main ridge of the ice cap experienced predominant thickening over 1994–1999 while areas to the south-east experienced thinning. Similar patterns were derived from ICESat observations for the more recent period 2003–2009 (Bolch et al., 2013; Rinne et al., 2011).

The characteristic NW-SE elevation change pattern of FIIC was first suggested to be driven by regional climate variability (Krabill et al., 2000). Predominant northwesterly winds push cold and dry Arctic air masses up the slope of FIIC toward warmer and more humid air over the northern Atlantic Ocean (Rasmussen, 2004). This confluence of air masses over the ice cap leads to higher precipitation on the northwestern windward side as compared to the southeastern leeward side. Over the 21st century, a persistence of this pattern of higher accumulation in the Northwest and predominant ablation in the Southeast can be expected. The combination of further rising air temperatures and projected increases in precipitation across northeast Greenland (Lenaerts et al., 2020) will likely trigger a development toward higher annual exchange at the glaciers in this region (Machguth et al., 2013), something that has also been suggested previously for other Arctic regions (e.g., Möller & Schneider, 2015).

However, more detailed analyses of the elevation change patterns of FIIC revealed that the NW-SE gradient is mainly driven by thickening in the upper regions of the two large, northwesterly outlet basins 2 and 3 of the ice cap (Figure 1). Rinne et al. (2011) found local thickening rates of up to 3.4 ± 0.7 m a^{-1} during 2004–2008. Such high increases of surface elevation are rare across Greenland and have only been observed at two surging outlet glaciers of the Greenland ice sheet during a quiescent phase (Pritchard et al., 2009). Similarly, basins 2 and 3 of FIIC were also suggested to be of surge type: Early observations from aerial photography revealed maximum ice flow velocities of 360 m a^{-1} (basin 2) and 175 m a^{-1} (basin 3) over the period 1961–1978 (Higgins, 1991). Comparable magnitudes of ice flow were also inferred to have occurred in the mid-1990s (Palmer et al., 2010), but then a substantial slowdown was observed toward 2005/2006 with basin 2 showing reduced velocities of <60 m a^{-1} and basin 3 being almost stagnant (Joughin et al., 2010). This chronology suggests the ending of a surge of basins 2 and 3 (Cook, 2016). It also suggests that the thickening, which was observed in the upper parts of basins 2 and 3 over 2004–2008, might be a "dynamic recovery" of the ice masses from the increased mass losses by ice discharge during the previous surge phase (Rinne et al., 2011). More recent CryoSat-2 observations (2010–2017) indicated a continuation of this recovery, although at lower rates of up to 2.4 ± 0.1 m a^{-1} (Kappelsberger et al., 2021).

However, basins 2 and 3 of FIIC are of particular interest not only because of their surge type characteristics and their dominating role in the elevation change pattern of the ice cap, but also because of their shared ice shelf. In the early days of Arctic glaciology, an undulating ice surface characteristic of floating ice was reported in the northwestern part of FIIC (Koenig et al., 1952). In combination with an observed disintegration of the glacier into flat-topped icebergs in this region (Helk & Dunbar, 1953), basins 2 and 3 were finally suggested to form floating tongues (Higgins, 1991). The assumption of flotation in basin 2 was later supported by sea water-salinity analysis at the western margin of its marine glacier terminus, which suggested the existence of a 45 m thick floating ice shelf in this region (Bendtsen et al., 2017). Flotation in basin 3 was also inferred from continuously low 2007 surface elevations across its terminus (Palmer et al., 2010).

Ice shelves in Greenland and the wider Arctic are rare (Cogley et al., 2011), as are surges of ice shelf terminating glaciers in general. In Antarctica, by contrast, ice shelves are numerous, so a full documentation and an understanding of the developments in basins 2 and 3 of FIIC are significant not only for the local and regional scopes, but also beyond. However, until now a lack of knowledge regarding processes at the grounding lines of the two basins has hampered this full understanding. The aim of this study is to contribute to closing this gap by conducting an in-depth analysis of the marine-terminating parts of the major drainage basins 2 and 3 of FIIC. We analyzed grounding line migration over recent decades using a range of proxy observations, which were derived from optical satellite images and radar interferometry. We further analyzed ice discharge variability between 1988 and 2020 using ice thickness cross sections along idealized flux gates and ice flow velocity from various remote sensing datasets. Based on our findings, we discuss potential reasons and triggers for the observed surges. We further discuss the role of the shared ice shelf in front of basins 2 and 3 for grounding line stability and for the future evolution of FIIC.

2. Data

For our analysis we used different types of data acquired during the period 1988–2021. For estimation of grounding line locations and determination of idealized flux gate locations we used optical satellite images and radar remote sensing data. For calculation of ice thicknesses and determination of buoyancy conditions we used different topographic datasets. For analysis of ice flow velocity and the subsequent calculation of ice discharge, we referred to various types of existing remote sensing-based datasets. Uncertainties of all these data are outlined and discussed in Section 4.

2.1. Grounding Lines

For estimating the grounding line locations from optical satellite data, we used Landsat scenes (30 m horizontal resolution) from five selected summers within the period 1993–2019 (Table S1 in the Supporting Information S1). We relied on true-color composites (red, green and blue bands) of each scene as these were best suited for visual interpretation. Our selection of five summers picked out the very limited number of scenes without cloud coverage that had enough surface contrast to allow for this visual interpretation. For estimating the grounding line locations based on radar remote sensing data, we used two triplets of subsequent Seninel-1 SAR (Synthetic Aperture Radar) images in SLC (Single Look Complex) format, acquired in IW- (Interferometric Wide swath) mode during the wintertime of 2018 and 2021 (Table S2 in the Supporting Information S1).

2.2. Elevation and Ice Thickness

We used gridded (2 m) surface elevations from the ArcticDEM strip product (https://doi.org/10.7910/DVN/OHHUKH, (Porter et al., 2018)), gridded (150 m) subglacial bed elevations from the BedMachine v3 data set (BM3, https://doi.org/10.5067/2CIX82HUV88Y, (Morlighem, et al., 2017a, 2017b) and surface and bed elevation profiles (25 m along-track resolution, 4.5 m vertical resolution) from the IceBridge MCoRDS L2 Ice Thickness, Version 1 data set (OIB, https://doi.org/10.5067/GDQ0CUCVTE2Q, (Paden et al., 2010)). ArcticDEM strips have been automatically created from high-resolution WorldView satellite imagery of specific dates (Noh & Howat, 2015) and have been applied in ice discharge calculations in previous studies (Mankoff et al., 2020; Sánchez-Gámez et al., 2019). We used three different strips from April/May 2013 for our analyses (Figure S1 in the Supporting Information S1). BM3 bed elevations have been created by subtracting a spatially extrapolated comprehensive compilation of various ice thickness measurements representing the period 2003–2009 from the surface elevations of the digital elevation model of the MEaSUREs Greenland Ice Mapping Project (GIMP) (Morlighem, et al., 2017a). Across basins 2 and 3 of FIIC, the BM3 ice thicknesses have mainly been created by kriging based on fixed zero thickness information at glacier margins and high-resolution thickness measurements along two longitudinal profiles (Figure 1) (Morlighem, et al., 2017a). These profiles have been measured by an Operation IceBridge flight on 6 May 2015 and are the same that are directly provided in the OIB data set that we also employed in our analysis. Both, ArcticDEM and OIB elevation data represent WGS84 ellipsoidal heights, which we converted to orthometric heights using the EGM2008 geoid (Pavlis et al., 2012). Figure 2 gives an overview of surface and bed elevations across the study area.

2.3. Ice Flow Velocity

For obtaining surface ice flow velocities we referred to various datasets and sources (Figure 3). The earliest part of the study period (1988–1992) and a part close to its end (2014–2018) are represented by annual Landsat-based ITS_LIVE velocity mosaics (https://doi.org/10.5067/6II6VW8LLWJ7; (Gardner et al., 2018, 2019)) with a resolution of 240 m. For the period between 1992 and 2014, the automatically generated ITS_LIVE mosaics were deemed error-prone across large parts of FIIC because of the patchy distribution of values across the velocity grids combined with physically unrealistic flow magnitudes in some locations and large areas of void data. Physically unrealistic magnitudes are also present in the 1988–1992 velocity mosaics, but almost exclusively along the close-to-stagnant ice divides. As the areas with questionable data do thus not overlap with our study area (and in absence of alternative data), we still used these ITS_LIVE mosaics (1988–1992) for the earliest years of our study period.

The winter 1995/1996 (January 2/3, 1996 to February 6/7, 1996) is represented by a 100 m resolution DInSAR (Differential Interferometric SAR) derived velocity field created on the basis of ERS-1/2 SAR data that were acquired during the tandem-mission period of the two satellites (Palmer et al., 2010). The winter 2000/2001, the five winters between 2005 and 2010 and the winter 2012/2013 are represented by 500 m resolution velocity fields that are part of the multiyear data set MEaSUREs Greenland Ice Sheet Velocity Map from InSAR Data, Version 2 (https://doi.org/10.5067/OC7B04ZM9G6Q; (Joughin et al., 2010, 2015)). This data set has been produced by applying both DInSAR and intensity tracking to radar images from various radar satellite missions.

The most recent years observed are represented not only by the ITS_LIVE velocity mosaics described above, but also by two additional datasets. The period December 2014 to November 2019 is covered by five 200 m resolution annual velocity mosaics that are part of the data set "MEaSUREs Greenland Annual Ice Sheet Velocity Mosaics from SAR and Landsat, Version 2" (https://doi.org/10.5067/TZZDYD94IMJB; (Joughin, 2010, 2020)). For the

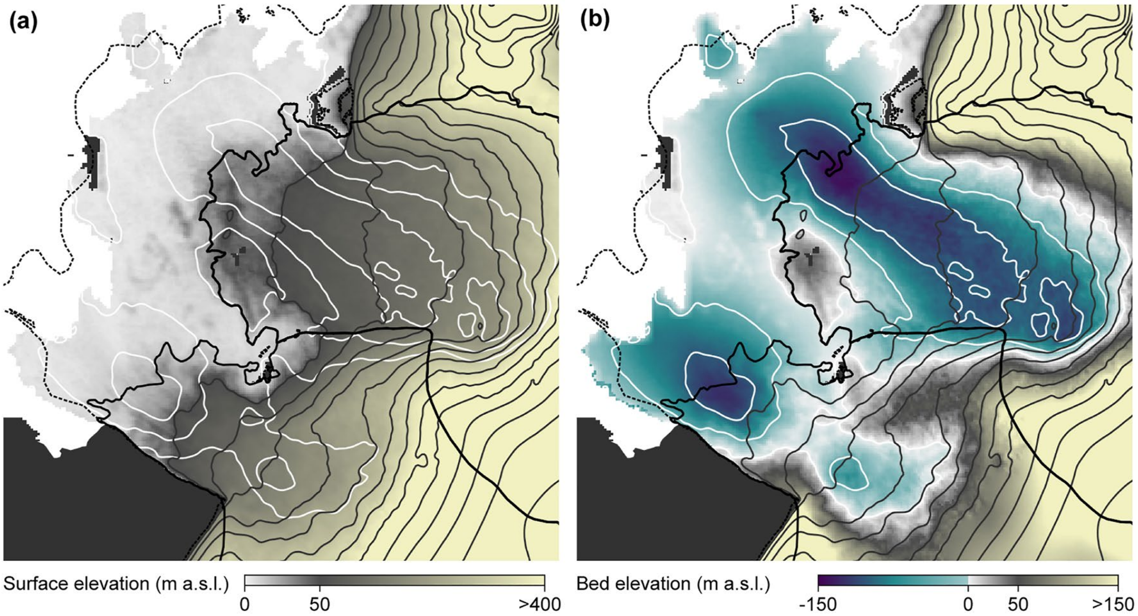

Figure 2. ArcticDEM surface elevations from 2013 (a) and BedMachine v3 based bedrock elevations (b). Submarine bedrock contours (white) and surface contours (dark gray) are displayed with a 50 m spacing in b panels. Basin boundaries (thick black lines) are shown along with the overall RGI 6.0 (Pfeffer et al., 2014) ice cap outline (thick dashed line). The basin boundaries include the 2018 grounding line (cf. Figure 4f). Each panel has edge lengths of 30 km.

years 2015–2020, we derived 200 m resolution annual velocity mosaics by averaging ~600 scene-pair velocity fields calculated by applying intensity tracking on >700 Sentinel-1 SLC IW acquisitions between January 2015 and December 2020 (Table S3 in the Supporting Information S1, Section 3.4). The GIMP DEM, resampled to 200 m spatial resolution (Howat et al., 2014) was used as a topographic reference for geocoding and orthorectifying the Sentinel-1 velocity fields, as well as for transferring the displacement from slant-range into ground-range geometry.

Apart from these velocity fields with specific annual assignment, the period December 1995 to October 2015 is additionally represented by the 250 m resolution mean annual velocity field provided in the MEaSUREs Multi-year Greenland Ice Sheet Velocity Mosaic, Version 1 (https://doi.org/10.5067/QUA5Q9SVMSJG; (Joughin et al., 2016, 2018)).

3. Methods

Our methodology is broken into four parts: (a) calculation of the Sentinel-1 annual surface ice flow velocity mosaics; (b) exact delineation of basins 2 and 3 of FIIC; (c) separation into the respective grounded and floating parts; (d) calculation of ice discharge through idealized flux gates.

3.1. Calculation of Sentinel-1 Annual Surface Velocity Mosaics

We produced six annual ice surface velocity mosaics of FIIC for the years 2015–2020 by averaging dense time series of Sentinel-1 scene-pair velocity fields (Table S3 in the Supporting Information S1). Scene-pair velocity fields were derived by applying a well-established intensity tracking algorithm that allows for both feature and speckle tracking (Friedl et al., 2018, 2021; Seehaus et al., 2018; Strozzi et al., 2002; Wegmüller et al., 2016; Wendleder et al., 2018) to subsequent pairs of more than 700 Sentinel-1 SLC IW repeat-pass SAR acquisitions. Over FIIC, Sentinel-1 repeat-pass imagery was available at a minimum time interval of 12 (2015 to mid-2016) and 6 (mid-2016 to 2020) days. We calculated velocities for these image intervals and time separations of up to 24 days, if no other data were available. The tracking window size was chosen to be 250 pixels in the range direction and 50 pixels in the azimuth direction, and the tracking step size was 50 × 10 pixels in range and azimuth. In order to remove unreliable measurements from the scene-pair velocity fields, measurements were discarded if their cross-correlation peak coefficient was <0.08. The value was determined empirically and offers a good

10.1029/2021JF006302

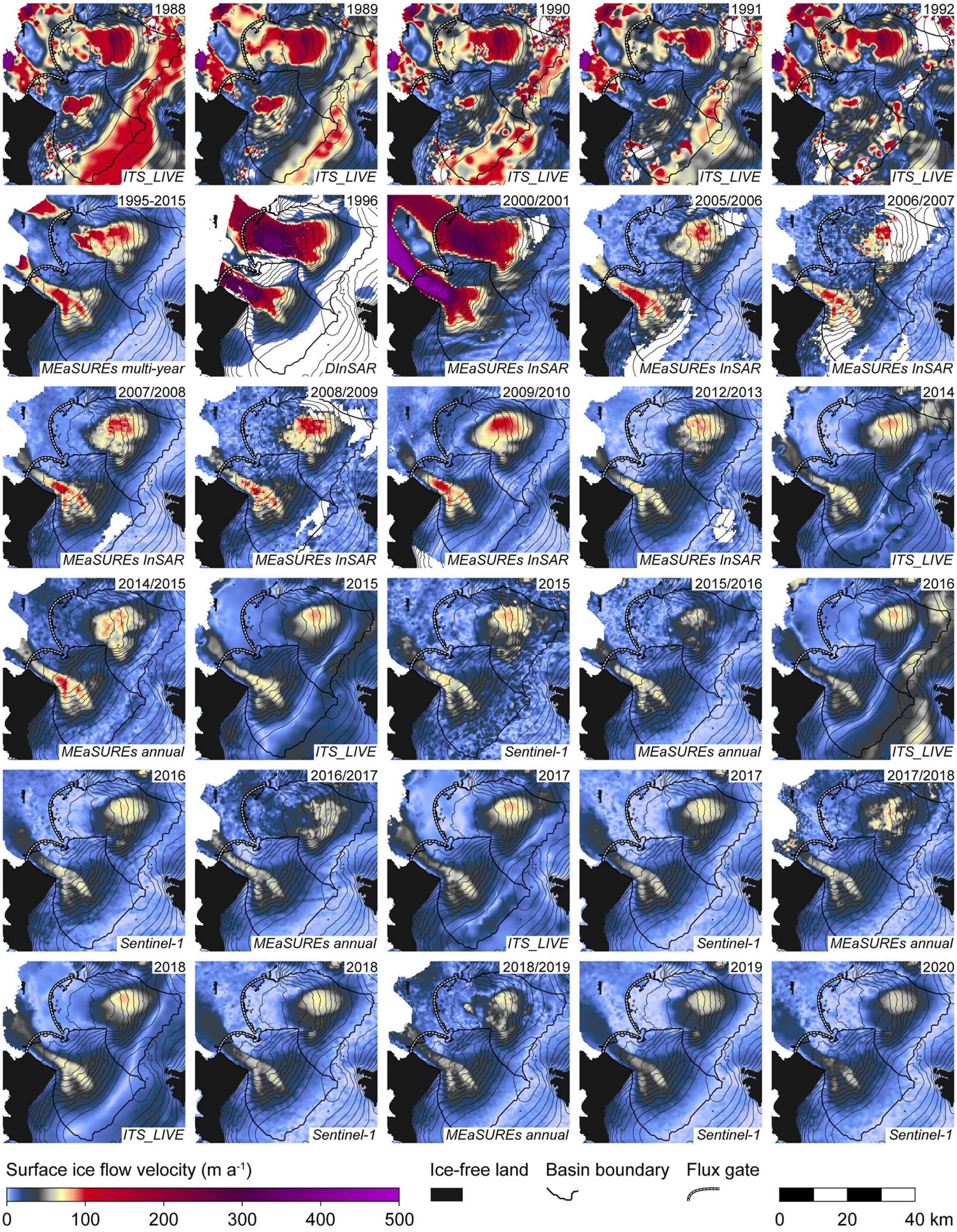

Figure 3. Overview of surface ice flow velocities used in the analysis (cf. Section 2). For each panel, temporal coverage (upper right) and the product type (lower right) are given. Surface ice flow velocity magnitudes are restricted to glacier boundaries of the MEaSUREs Greenland Ice Mapping Project (GIMP) Land Ice and Ocean Classification Mask V1. The flux gates of basins 2 and 3 (thick black curves) are shown on top of the basin boundaries (thin black outlines; cf. Figure 1b and Section 3.2). The basin boundaries include the 2018 grounding line (cf. Figure 4f).

balance between eliminating very bad blunders and keeping valid measurements (Friedl et al., 2021). However, as this step offers just a pre-filtering of the data, precise and final filtering is performed for each individual velocity field using a three-step filter of Lüttig et al. (2017). This filter strategy removes more than 99% of erroneous data points, while keeping a maximum of valid velocity measurements, and comprises filtering based on (a) a priori velocity information, (b) a median velocity filter and (c) a directional filter. As a priori velocity information for our 2015–2018 velocity data, we used the corresponding ITS_LIVE annual velocity mosaics of the same year and for all velocity fields in 2019 and 2020, we used the latest available ITS_LIVE annual velocity mosaic from 2018. After filtering, we corrected our Sentinel-1 velocity fields for any remaining co-registration errors (mean - value <4 m a^{-1} for the velocity's magnitude) by calibrating our range and azimuth velocities against median velocities measured over ice-free ground. Finally, each velocity field was labeled with a specific time stamp, computed as the mean of the two acquisition dates of the input data.

Using all Sentinel-1 scene-pair velocity fields with a time stamp between 1 January and 31 December of each year and taking the individual SNR (signal-to-noise ratio) of the measurement pixels as weights, we computed annual velocity mosaics by calculating the weighted mean of each velocity component and the velocity magnitude. Before calculating the weighted mean, the azimuth and range velocities of the scene-pair velocity fields were converted into x (East-West) and y (North-South) velocity components and measurements were removed if the velocity in one of the two directions deviated from the pixel-stack's median by more than two times the standard deviation (Mouginot et al., 2017). For more detailed information on the procedures of Sentinel-1 scene-pair velocity field generation and annual mosaicking, we refer to Friedl et al. (2021).

3.2. Delineation of Basins 2 and 3

We delineated the boundaries of basins 2 and 3 in the interior of FIIC by manual digitization based on combined information drawn from surface ice flow velocities in the Sentinel-1 2019 mosaic and ArcticDEM surface elevations (Figure 1b). Such a combination of elevation and velocity data for identification of basin boundaries has been proven successful before (e.g., Mouginot et al., 2015, 2019; Krieger, Johnson, & Floricioiu, 2020).

The delineation followed a three-step workflow: (a) Boundaries were drawn along drainage divides that are clearly identifiable from surface elevations. (b) As ice flow direction may start to differ from pure down-slope directions with increasing flow velocity (Krieger, Floricioiu, & Neckel, 2020), we identified lines of diverging ice flow as additional criterion for boundary delineation. The hereby used ice flow directions were derived from the x- and y-vectors of the Sentinel-1 velocity data. (c) We corrected the rather straight elevation-based drainage divides according to the less straight flow direction-based divides.

Differing from this overall workflow, the lowermost part of the boundary between basins 2 and 3 was drawn along a line of ice flow confluence (Figure 1b). In this area, the ice from both basins blocks each other from lateral spreading and starts to merge into a unified ice mass that finally forms the shared ice shelf.

3.3. Separation of Floating and Grounded Ice

In general, the transition between grounded and floating ice of a glacier occurs across the so-called grounding zone (Friedl et al., 2020; Vaughan, 1995). At the landward end of this zone, that is, at the hinge line, the ice body is still grounded, but starts to be influenced by tidal flexure. At the seaward end, the ice shelf becomes freely floating. The true grounding line, where the ice detaches from the ground, lies somewhere in between. For separating basins 2 and 3 into floating and grounded parts we localized the approximate grounding lines by applying one dynamic and two static remote sensing methods for grounding line proxy mapping: the tidal method, the surface slope method and the hydrostatic method (Friedl et al., 2020). With our grounding line analysis, we cover eight specific dates between 1993 and 2021 and thus most of the study period (Figure 4).

Using double-difference interferograms, derived by applying a DInSAR-technique on two consecutive triplets of 6-day repeat Sentinel-1 IW SLC acquisitions ((Friedl et al., 2020), Table S2 in the Supporting Information S1), we manually mapped the upstream limit of tidal flexure, that is, the hinge line, for the years 2018 and 2021 which appears as a dense edge area between floating and grounded ice (Figures 4f and 4h). This type of grounding line proxy usually lies slightly seaward of the true hinge line and is therefore assumed to be close (±100 m) to the true grounding line (Friedl et al., 2020). The radar-derived proxies are the only ones in our study that allowed

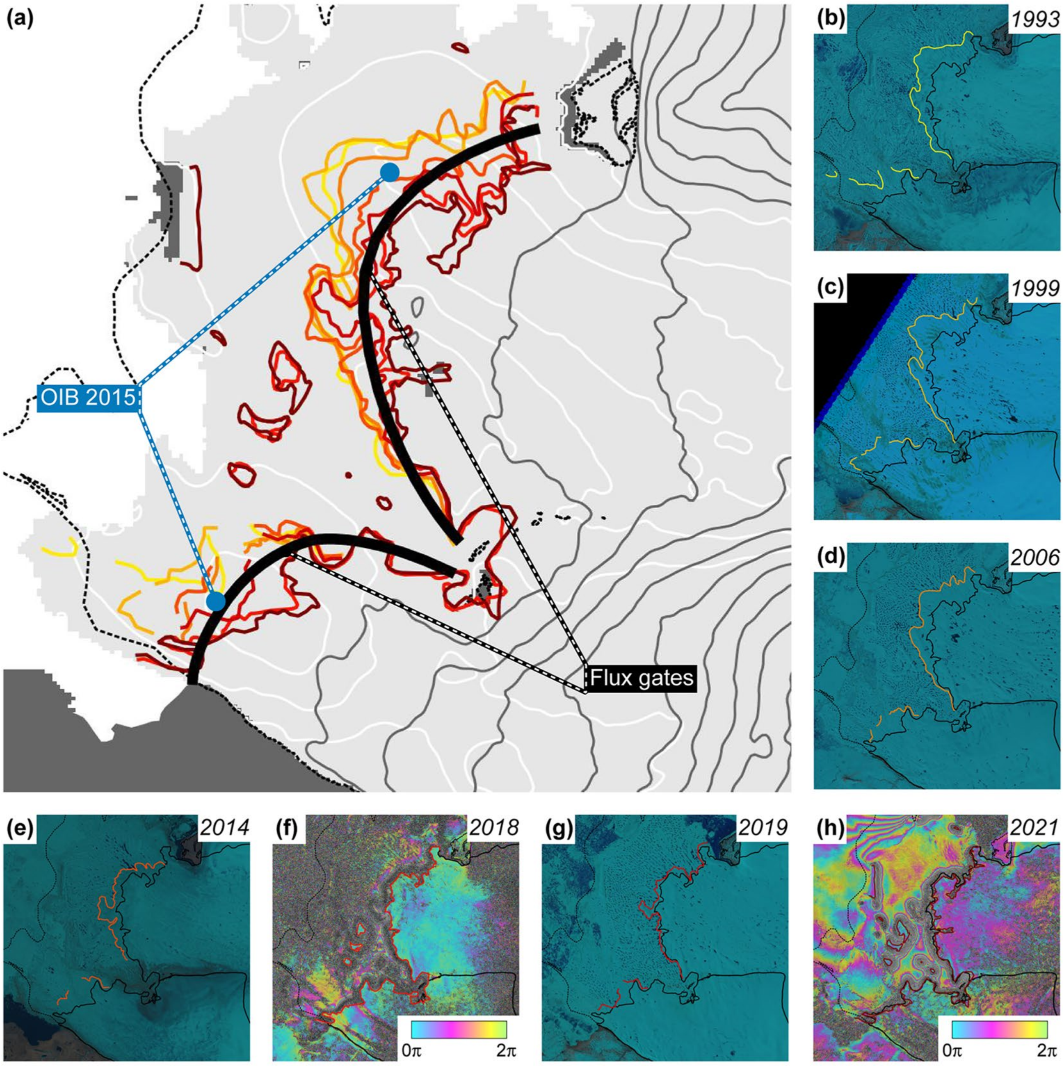

Figure 4. Overview of grounding line proxies (cf. Section 3.3) and locations of the idealized flux gates in basins 2 and 3 (cf. Section 3.4). In (a), all grounding line proxies are combined (keeping their individual color code from panels b–h) and the idealized flux gates are shown as thick black curves. OIB-derived grounding line proxies are marked by blue dots (cf. Figures 5b and 5c). BedMachine v3 based submarine bedrock contours (white) and surface contours (dark gray) have a 50 m spacing. Details about the satellite images (b-e, g) and radar double-difference interferograms (f), (h) from which the different proxies were derived are given in Tables S1 and S2 in the Supporting Information S1. The interferograms also identified isolated regions of grounded ice within the continuous ice shelf in front of basins 2 and 3. In all panels, the outlines of basins 2 and 3 (thick black lines) are marked along with the overall RGI 6.0 ice cap outline (dashed black line). Note that the 2018 grounding line is used as the seaward part of the basin boundaries in all panels. Each panel has edge lengths of 30 km.

for a determination of continuous grounding lines across basins 2 and 3, including the transitional area between both basins.

On the basis of a visual inspection of true-color composites of five Landsat images (Table S1 in the Supporting Information S1), we approximated the grounding line locations for the years 1993, 1999, 2006, 2014 and 2019 (Figures 4b–4e and 4g). Following the surface slope method, we manually digitized breaks in surface topography that were visually identifiable as well-defined changes in brightness values (e.g., Brunt et al., 2010; Scambos et al., 2007). This type of grounding line proxy tends to be located seaward from the true grounding line. It is generally less accurate than DInSAR-derived grounding line proxies, but offers the great advantage of a longer duration of data coverage (Le Meur et al., 2014). It has thus been regularly applied in grounding line mapping (e.g., Bindschadler et al., 2011; Christie et al., 2016). Moreover, where the break in surface slope is well

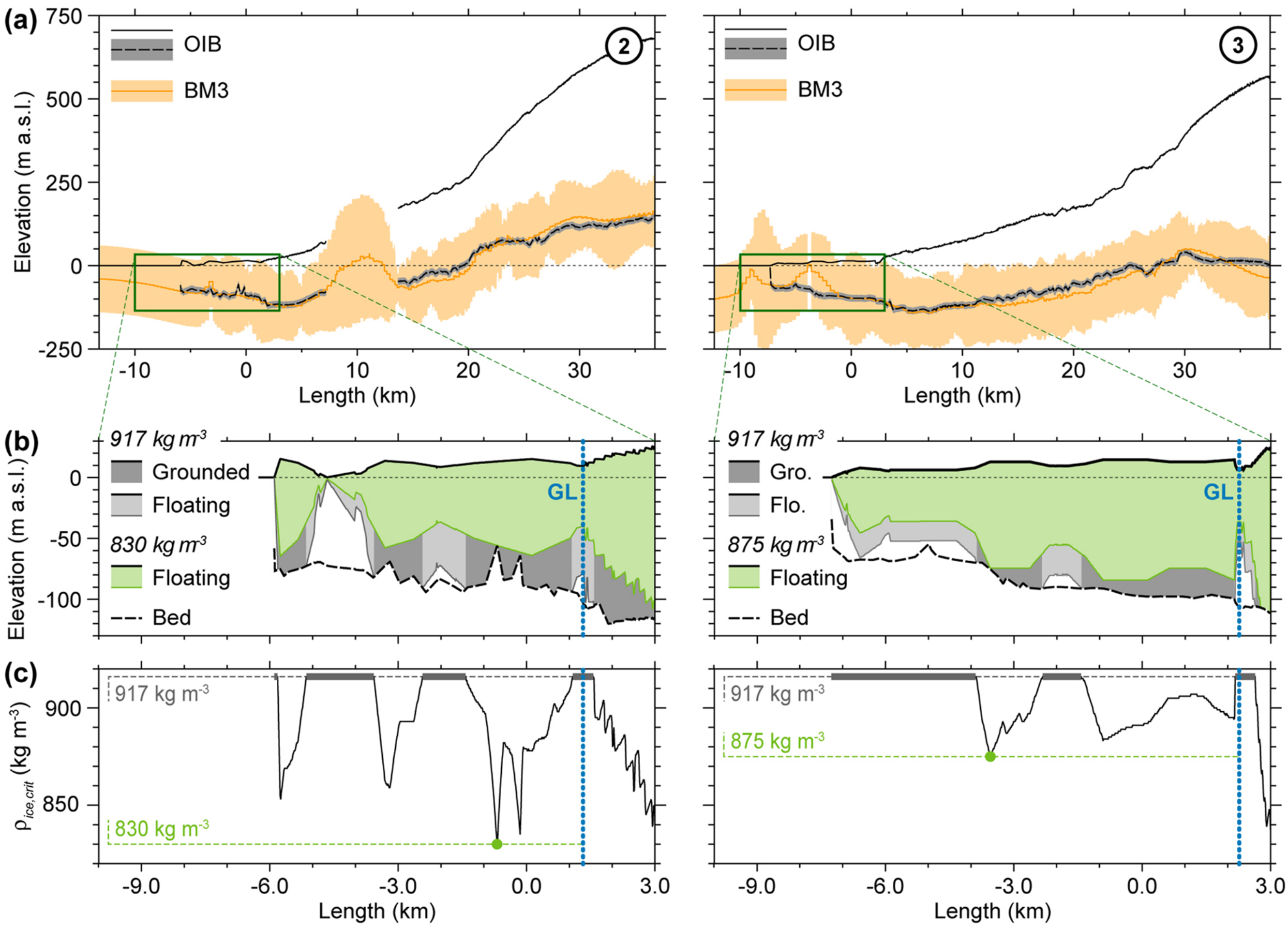

Figure 5. Profiles of basins 2 and 3 along the Operation IceBridge flight tracks shown in Figure 1a. The complete along-basin profiles of glacier surface and bed according to IceBridge MCoRDS (OIB) data and of the glacier bed according to BedMachine v3 (BM3) data are shown in (a). Bed elevations of both datasets are shown together with the respective uncertainty ranges. The dark green insets mark the locations of the profile sections detailed below. Detailed profiles of the ice shelf with thicknesses according to different ice density assumptions are shown in (b). The maximum glacier ice density that allows for flotation at the respective section of the profile ($\rho_{\mathrm{ice,crit}}$) is shown in (c). In (b) greyish colors represent the ice shelf as it would look under the standard glacier ice density assumption. Light and dark gray colors distinguish between floating and grounded shelf ice. In (c) sections of the profiles that are afloat independent of any density assumption (i.e., $\rho_{\mathrm{ice,crit}} = 917$ kg m^{-3}) are marked by thick gray bars. The dashed green line indicates the minimum $\rho_{ice,crit}$ that is needed to allow for continuous flotation along the respective ice shelf profile. In (b) the greenish colors represent the ice shelf as it would look under the assumption of these minimum $\rho_{\mathrm{ice,crit}}$ along the entire profiles. Derived grounding line locations for each basin are indicated in blue. The *x*-axis corresponds to grounding line variability according to Figure 7.

developed or where relatively slow moving ice is present (as is the case for basins 2 and 3 of FIIC), the surface slope method is typically in good agreement with DInSAR estimates (Friedl et al., 2020; Rignot et al., 2011). The spatial extent of the Landsat-based grounding line proxy covers the entire widths of the two basins, except for the transitional area between both basins, where mapping was prevented by a lack of visual contrast for tracking features.

In addition, we used buoyancy calculations on OIB data to identify floating shelf ice sections along the OIB flight tracks (Figure 5) and then used the upstream boundaries of these sections as a proxy for the approximate grounding line locations in 2015 (Figure 4a). As for the surface slope method, the proxies derived with this hydrostatic method are usually located slightly seaward from the true grounding lines (Friedl et al., 2020), but can reach deviations of up to 10 km in single cases (Brunt et al., 2010). In general, buoyancy calculations require reliable information about mean glacier densities, especially in the context of limited water depths and potential firn coverage. Following Friedl et al. (2020), we first applied standard densities for glacier ice ($\rho_i = 917$ kg m^{-3}) and sea water ($\rho_w = 1{,}027$ kg m^{-3}) across the areas of submarine bedrock elevations (Figure 5). Assuming freely floating ice, we calculated ice thickness in hydrostatic equilibrium (h_{eq}) according to OIB ice surface elevation (e_{surf}):

$$h_{\mathrm{eq}} = \frac{e_{\mathrm{surf}}}{1 - \frac{\rho_i}{\rho_w}} \tag{1}$$

By comparing h_{eq} to OIB ice thickness we aimed to identify floating shelf ice sections, but found large sections of grounded ice (Figure 5). However, as evidence from previous studies strongly suggests the ice shelf is floating, we considered that the ice shelf density is likely to be lower than the maximum value used above. Hence, we calculated critical glacier ice densities $\rho_{ice,\mathrm{crit}}$ along the OIB flight tracks that are required to allow for flotation of the respective shelf ice section (Figure 5) and then considered their feasibility.

3.4. Calculation of Ice Discharge

The mapped grounding line proxies inevitably differ somewhat from the location of the true grounding line (Friedl et al., 2020). Additionally, their shape is spatially varied across basins 2 and 3 and their positions vary over time (Figure 4). Therefore, it was necessary to define idealized flux gates for our ice discharge calculations. These flux gates follow a spatiotemporally averaged shape of the different grounding line proxies (Figure 4a). Because the grounding lines retreated over time, the idealized flux gates are situated landward of the true grounding lines during the earlier part of the study period, while during the later part they are situated seaward of them.

We calculated ice discharge (D) through these idealized flux gates by integrating the product of ice thickness (h) and vertically averaged ice flow velocity perpendicular to the flux gate ($\bar{v}$) over the distance across the respective flux gate cross section (x) (Figure 6) according to:

$$D = \int_x (h \cdot \bar{v})\, dx \tag{2}$$

Values from the different datasets were sampled at a 100 m spacing in the x direction. Ice thickness was calculated using BM3 bed elevations and ArcticDEM surface elevations from April/May 2013 (Figure 2). The calculation of $\bar{v}$ was a two-step process. First, we calculated surface ice flow velocity perpendicular to the respective part of the flux gate ($v_{\mathrm{surf}}(x)$). To do so, we reduced the velocity magnitudes from the various velocity datasets (cf. Figure 3) according to the sine of the spatially varying angle between the ice flow direction and the orientation of the flux gate (Vijay & Braun, 2017, Figure 6). The ice flow direction of the 1995–2015 MEaSUREs Multi-year Greenland Ice Sheet Velocity Mosaic, Version 1 (cf. Section 2) was considered representative of the entire study period. We then calculated $\bar{v}$(x) by multiplying $v_{\mathrm{surf}}(x)$ with a constant factor of 0.9:

$$\bar{v}(x) = 0.9 \cdot v_{\mathrm{surf}}(x) \tag{3}$$

This assumption is justified as vertically averaged ice flow velocity can generally be approximated as a composite of surface (v_s) and basal velocity (v_b):

$$\bar{v} = \frac{4}{5} v_s + \frac{1}{5} v_b \tag{4}$$

It is thus confined to 80%–100% of surface flow velocity, depending on the level of basal sliding present under the glacier (Cuffey & Paterson, 2010). In the case of minimum basal sliding ($v_b = 0$) $\bar{v}$ equals 80% of v_s and in the case of maximum basal sliding ($v_b = v_s$) $\bar{v}$ equals 100% of v_s. The factor of 0.9 (i.e., 90% of v_s) mediates between these extreme values.

We performed the calculations of vertically averaged ice flow velocity perpendicular to the flux gate and subsequently of ice discharge itself separately for each velocity data set (cf. Figure 3). For the final conversion of ice volume to mass, we used a density of glacier ice of 875 kg m^{-3} which we derived from the OIB buoyancy calculations (Figure 5). A reduction of glacier ice density to at least this value was necessary to allow for flotation of the ice shelf in front of basin 3. Assuming this same density for the ice shelf in front of basin 2, resulted in limited sections of grounded ice at isolated spikes in the bedrock topography. As those spikes can likely be seen as artifacts, resulting from misinterpretation of radar echograms during creation of the OIB data, it can be assumed that a glacier ice density of 875 kg m^{-3} also allows for flotation of the ice shelf in front of basin 2. This value is lower as the standard glacier ice density (917 kg m^{-3}) usually assumed in ice discharge calculations (e.g., Mankoff et al., 2020). However, it is well within the range of possible glacier ice densities, which may be as low as 830 kg m^{-3}

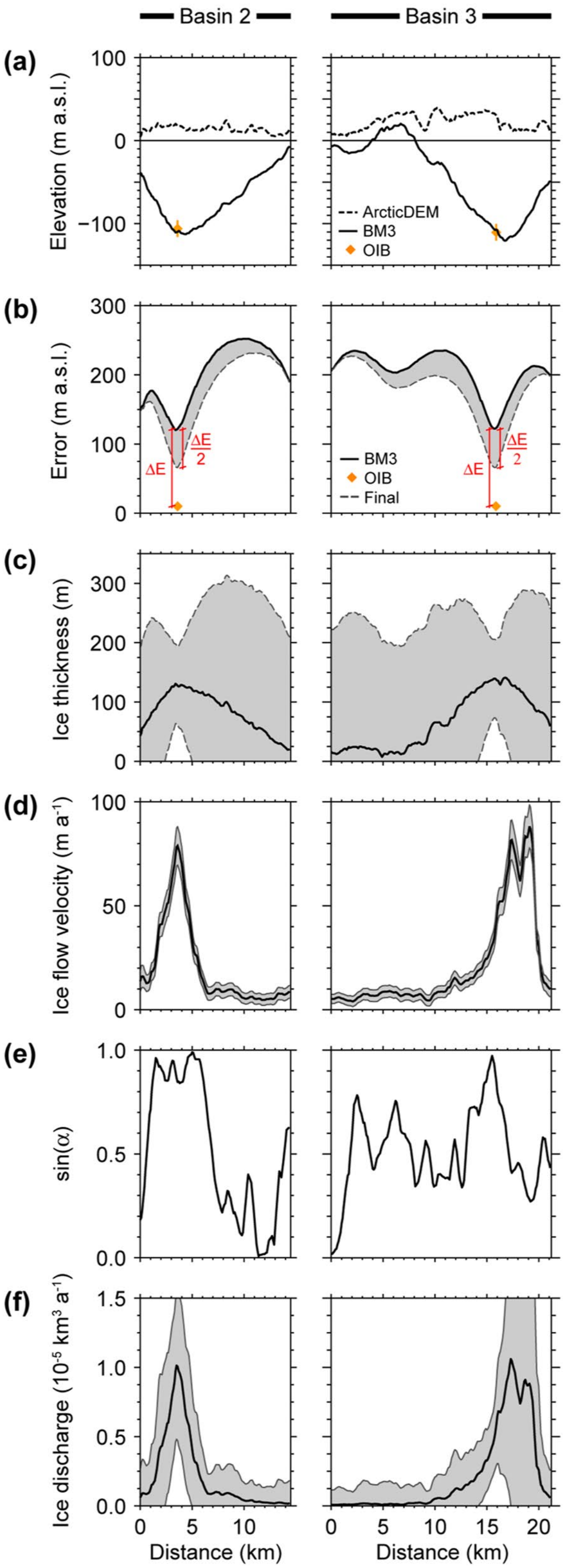
Basin 2
Basin 3
(a)
Elevation (m a.s.l.)
100
0
−100
ArcticDEM
BM3
OIB
(b)
Error (m a.s.l.)
300
200
100
0
ΔE
ΔE/2
BM3
OIB
Final
(c)
Ice thickness (m)
300
200
100
0
(d)
Ice flow velocity (m a⁻¹)
100
50
0
(e)
sin(α)
1.0
0.5
0.0
(f)
Ice discharge (10⁻⁵ km³ a⁻¹)
1.5
1.0
0.5
0.0
0
5
10
15
20
Distance (km)
Distance (km)

Figure 6.

in the case of heavily crevassed ice (Cuffey & Paterson, 2010). It also fits well with density data from an ice core drilled near the summit of FIIC in 2006, which show densities of down to almost 800 kg m^{-3} at depths of more than 30 m (Simonsen et al., 2013). Finally, our usage of surface elevations from a late spring/early summer season in the calculation of the flux gate cross sections, which implies firn-covered glacier ice, also supports the assumption of a reduced glacier ice density.

4. Uncertainty Assessment

For the assessment of uncertainties related to our calculations of ice discharge, we focused on the grounding zones of basins 2 and 3. We considered all types of uncertainties that influence ice thickness or ice flow velocity across the two flux gates. These uncertainties are partly dataset-related and partly related to our calculation methods.

4.1. Topographic Uncertainties

Uncertainties resulting from topography-related issues are mainly based on the uncertainty ranges of the surface and bed elevation datasets. The surface elevations of the ArcticDEM strip product show uncertainties of below 4 m in general, which may even reach sub-meter scale in the case where optimal ground control points have been used during creation of the product (Noh & Howat, 2015). The OIB surface elevations have generally low uncertainties of ±0.1 m (Krabill et al., 2002). The BM3 bed elevation uncertainty grid ($U_{\mathrm{bed,BM3}}$), which is provided together with the bed elevation grid, shows uncertainties that largely exceed the derived ice thickness across the flux gates, but also across basins 2 and 3 in general (Figure 6). This is because the poor sampling of measurements across FIIC failed to constrain kriging and interpolation efforts that formed the basis for the creation of BM3 bed elevations across the ice cap (Morlighem, et al., 2017a, 2017b). The high resolution OIB bed elevations show an uncertainty of just $U_{\mathrm{bed,OIB}} = 10$ m (Li et al., 2013). As these data profiles have been used in the creation of the BM3 bed elevations, BM3 and OIB bed elevations are rather similar along the OIB flight tracks (Figure 5) and BM3 bed elevation uncertainties are minimal (Figure 6). Root mean square differences between BM3 and OIB bed elevations below the ice shelf amount to just ±8.9 m a.s.l. (basin 2) and ±25.3 m a.s.l. (basin 3) and largely trace back to isolated bumps (cf. Figure 5) in either, but not both of the two datasets. This gives additional confidence in the BM3 bed elevations along the OIB flight tracks and suggests that the BM3 bed elevation uncertainty grid considerably overestimates the actual uncertainties across the grounding zones of both basins. We therefore developed a construction scheme for bed elevation uncertainties across the flux gates that takes into account both BM3 and OIB uncertainties.

BM3 bed elevation uncertainties exceed BM3 ice thicknesses across both flux gate cross sections (Figure 6). However, BM3 bed elevations at the crossing points of the idealized flux gates and the OIB flight tracks lie within the small uncertainty range of ±10 m of the OIB bed elevations in both basins (Figure 6), suggesting that these BM3 bed elevations are likewise reliable. We consequently corrected the rather large $U_{\mathrm{bed,BM3}}$ by a conservative intermediary between the two inconsistent bed uncertainties (Figure 6) as follows: We considered a maximum correction of half the difference between BM3 and OIB bed uncertainties (ΔU_{bed}) at the crossing point ($x = P$) between OIB flight track and idealized flux gate at the respective basin:

$$\Delta U_{\mathrm{bed}}(P) = \frac{U_{\mathrm{bed,BM3}}(P) - U_{\mathrm{bed,OIB}}}{2} \tag{5}$$

We then constructed the final bed uncertainty across each flux gate cross section ($U_{\mathrm{bed}}(x)$; Figure 6) by reducing $U_{\mathrm{bed,BM3}}(x)$ according to:

$$U_{\mathrm{bed}}(x) = U_{\mathrm{bed,BM3}}(x) - \frac{\Delta U_{\mathrm{bed}}(P)}{P} x(for \quad x \in [0, P]) \tag{6a}$$

Figure 6. Workflow of ice discharge calculations across the idealized flux gates of basins 2 and 3. ArcticDEM surface and BedMachine v3 (BM3) bed elevations (a) were used as topographic data for calculation of ice thicknesses (c). Bed elevation uncertainties were created from BM3 and IceBridge MCoRDS (OIB) data ((b); cf. Equation 6) and were used as a measure of uncertainty for ice thicknesses. Vertically averaged ice flow velocities (d) and ice flow directions relative to the flux gate (e) were taken from the MEaSUREs 1995–2015 multiyear mosaic. The related velocity uncertainties were calculated according to Equation 9. A sine of 1.0 indicates ice flow that is perfectly perpendicular to the flux gate ($\alpha = 90°$). Ice discharge ((f), cf. Equation 2) is displayed along with its uncertainty, which was calculated according to Equation 10.

$$U_{\mathrm{bed}}(x) = U_{\mathrm{bed,BM3}}(x) + \frac{\Delta U_{\mathrm{bed}}(P)}{x_{\max} - P}\,(x - x_{\max})\,(for\;\; x \in [P, x_{\max}]) \tag{6b}$$

In addition to this quantifiable uncertainty, the weak constraint of the BM3 bed elevation construction by measured data in the area of FIIC (Morlighem, et al., 2017a, 2017b) potentially introduced additional uncertainty that cannot be quantified but needs to be considered.

The shape and depth of the subglacial troughs of basins 2 and 3 are largely based on measured OIB data and on ice free areas along the ice edges (Morlighem, et al., 2017a, 2017b). This means that the positioning of the OIB "glacier centerline" flight tracks (Figure 1a) partly determines the locations and elevations of the deepest known parts of the bed in the derived topographic data set. For basin 3, a comparison of these depth contours (Figure 2b) with the fast ice flow pattern (Figure 3) indicates a misalignment between the deepest parts of the subglacial trough and the region of fastest ice flow. This suggests that glacier cross sections in this area might underestimate the real depth of the trough and falsely localize its deepest parts.

Across the central parts of the downstream ice shelf, BM3 bed elevations are also error prone. The close-to-zero BM3 bed elevations suggest continuously grounded ice across the shelf ice areas between basins 2 and 3 (Figure 2b), when considering the decameter-scale thickness of the ice shelf (cf. Figure 5). However, the two Sentinel-1 DInSAR interferograms clearly indicate floating ice across large parts of this area and only a few isolated spots of grounded ice (Figures 4f and 4h). This suggests a significant but unquantifiable overestimation of bed elevations by BM3 data in this area, but also a potential misestimation of the flux gate cross section of basin 3.

Assuming a continuous subglacial bedrock, the described overestimation of sub-shelf bed elevations implies that the adjacent BM3 bed elevations above zero (Figure 2b), that are present across the southwestern part of the flux gate of basin 3 (Figure 6) might be subject to overestimation, too. However, supporting evidence for this bedrock feature also exists. Landsat scenes from 2006 to 2019 reveal an elongated convex terrain feature along the left part of the grounding zone of basin 3 (Figures 4d and 4g), that is also visible in the ArcticDEM surface elevation data (Figure 2a). Such a glacier surface feature strongly suggests the existence of a corresponding subglacial counterpart and a reduced ice thickness compared to surrounding areas. Accordingly, the constructed BM3 bed elevation data indicate a comparable bedrock feature (Figure 2b). Further following this chain of evidence, the ice flow pattern reveals a blocking of fast flow in this area (Figure 3). As such a strong decrease of the flow velocity over a very short distance can only be explained by a retrograde-sloping subglacial bed and a considerably reduced glacier cross section, it strongly supports the high bed elevations and reduced ice thicknesses across the left part of the flux gate of basin 3 (Figure 6) as a reliable feature. Assuming these high bed elevations are real, implies that the positioning of the OIB flight track along basin 3 (Figure 1a) is close to the central flow line and thus close to the deepest part of the subglacial trough across the grounding zone. This, in turn, gives additional confidence in the BM3 based ice thickness values of the deepest parts of the flux gate cross section of basin 3.

4.2. Uncertainty of Ice Flow Velocities

The different MEaSUREs and ITS_LIVE surface ice flow velocity datasets (Figure 3) include corresponding uncertainty grids ($U_{v,\mathrm{surf}}$), which show velocity uncertainties across basins 2 and 3 that are mostly at least an order of magnitude smaller than the actual velocity values. While the ice flow velocity ranges up to a couple of hundred meters across the fast-flowing regions in the central parts of basins 2 and 3 (Figure 3), the associated mean uncertainty only reaches ± 8.3 m a^{-1} on average across the two basins. For the DInSAR derived 1996 surface ice flow velocity field (Figure 3) we assume a constant uncertainty $U_{v,\mathrm{surf}} = \pm 7$ m a^{-1} (Palmer et al., 2010).

The uncertainty of the derived Sentinel-1 scene-pair velocity fields usually consists of two components: the uncertainty related to imprecise image co-registration and the uncertainty related to the tracking algorithm (Seehaus et al., 2015). As we corrected our Sentinel-1 scene pair velocity fields for co-registration uncertainties (cf. Section 3.1), we assume that the remaining velocity uncertainty e is mainly related to the algorithm's tracking accuracy of 0.1 pixel, the pixel size ps_r and $\mathrm{ps}_{\mathrm{az}}$ in each direction (3×14 m for Sentinel-1 IW SLC), as well as the temporal baseline tb of the image pair (Mouginot et al., 2017):

$$e = \sqrt{\left(\frac{0.1 * \mathrm{ps}_r}{\mathrm{tb}}\right)^2 + \left(\frac{0.1 * \mathrm{ps}_{\mathrm{az}}}{\mathrm{tb}}\right)^2} \tag{7}$$

This results in velocity uncertainties of 0.24 m d^{-1} (88 m a^{-1}) and 0.12 m d^{-1} (44 m a^{-1}) for Sentinel-1 IW data with a pixel size of 3 × 14 m, acquired at the typical repeat cycles of 6 and 12 days, respectively. Based on the uncertainties of the individual scene-pair velocity fields, we calculated the uncertainties of the annual Sentinel-1 velocity mosaics ($U_{v,\mathrm{surf}}$) as the weighted standard error for each pixel-stack. These standard errors (averaged across basins 2 and 3) range between 6.6 m a^{-1} (2018) and 25.8 m a^{-1} (2020) and lie thus in the same order of magnitude as the uncertainties of the MEaSUREs and ITS_LIVE velocity datasets.

In order to derive the final uncertainties of surface ice flow velocity of each data set ($U_{v,\mathrm{surf}}(x)$), we extracted profiles across the flux gates from the field-specific uncertainty grids of surface ice flow velocity and reduced them according to the sine of the spatially varying angle between ice flow direction and the orientation of the flux gate as was done during the calculation of $v_{\mathrm{surf}}(x)$ (cf. Section 3.4). In addition to $U_{v,\mathrm{surf}}(x)$ we quantified the uncertainties introduced by our conversion between surface ice flow velocity $v_{\mathrm{surf}}(x)$ and the vertically averaged ice flow velocity $\bar{v}(\mathrm{x})$. As the latter lies between 80% and 100% of the former (Equation 4), we applied a mediating factor of 0.9 (90%) in this conversion (Equation 3). In order to capture the full range of potential deviations (±10%), we considered an uncertainty due to velocity conversion ($U_{v,\mathrm{conv}}(x)$) of:

$$U_{v,\mathrm{conv}}(x) = 0.1 \cdot v_{\mathrm{surf}}(x) \tag{8}$$

By treating the two velocity-relevant uncertainties as independent from each other, we calculated the uncertainty of vertically averaged ice flow velocity perpendicular to the flux gate across each flux gate cross section ($\mathrm{U}\bar{v}(\mathrm{x})$) by combining them in quadrature:

$$U_{\bar{v}}(x) = \sqrt{U_{v,\mathrm{surf}}(x)^2 + U_{v,\mathrm{conv}}(x)^2} \tag{9}$$

We did not consider seasonal variability of ice flow velocity in our analysis.

4.3. Quantification of Ice Discharge Uncertainty

The uncertainty of our ice discharge calculations mainly depends on the individual uncertainties of bed elevation and vertically averaged ice flow velocity perpendicular to the flux gate. Accordingly, we calculated ice discharge uncertainty across each flux gate cross section ($U_D(x)$) from the individual uncertainties $U_{\mathrm{bed}}(x)$ (Equation 6) and $\mathrm{U}\bar{v}(\mathrm{x})$ (Equation 9) and on the basis of the related absolute values of ice discharge ($D(x)$), ice thickness ($h(x)$) and vertically averaged ice flow velocity perpendicular to the flux gate ($\bar{v}(x)$) by following standard error propagation rules:

$$U_D(x) = D(x) \cdot \left(\frac{U_{\mathrm{bed}}(x)}{h(x)} + \frac{U_{\bar{v}}(x)}{\bar{v}(x)}\right) \tag{10}$$

We neglected the minimal BM3 surface elevation uncertainty (cf. Section 4.1) and treated $U_{\mathrm{bed}}(x)$ (Equation 6) as the exclusive measure of the uncertainty in ice thickness.

It should be noted that we calculated ice discharge over a 32-year period (1988–2020) on the basis of time-invariant topographies, flux gates and ice flow directions. This means that we did not account for any changes in ice thickness during this period that likely occurred as a result of surface elevation changes (e.g., Bolch et al., 2013; Hugonnet et al., 2021). In our case, we regard this as more appropriate than an inclusion of ice thickness corrections as they were applied in previous ice discharge calculation (e.g., Mankoff et al., 2020; Sánchez-Gámez et al., 2019). These studies used known elevation change rates between dates with available surface elevation data for interpolation. However, for FIIC, surface elevation change rates are only available for the period since 2000 (Hugonnet et al., 2021). In addition, the strongly time-varying ice flow regimes (cf. Figure 3) suggest alternating periods of ice thinning and thickening, which complicate or even prohibit temporal extrapolation. We therefore opted for a time-invariant surface topography in order to maintain a consistent approach over our entire study period. Furthermore, we did not account for any changes of the flux gate cross sections that likely occurred as a result of grounding line retreat (cf. Figure 4a). This approach of using a single flux gate per basin is in line with previous ice discharge studies in Greenland (Enderlin et al., 2014; King et al., 2018), but implies either over- or underestimation of ice discharge volumes. If the flux gate is located upstream of the true grounding line, our calculated ice discharge overestimates the ice mass passing the true grounding line, as it includes all ice volume that would have been removed by surface melting across the area between the flux gate and the true grounding line. This effect was discussed by Mankoff et al. (2020) and was found to be negligible. Accordingly, if the flux gate is located downstream of the true grounding line, our calculated ice discharge does not include any ice volume that has previously been removed by basal submarine melting across the area between the true grounding line and the flux gate. We assume basal submarine melting to be as negligible as surface melting (cf. Mankoff et al., 2020) in this respect, and so do not account for either in our analyses.

We also excluded any temporal changes in ice flow direction through the flux gates that may have occurred with variations in ice flow dynamics over time (cf. Figure 3). Areas of fast ice flow show flow directions almost perpendicular to our idealized flux gates (cf. Figure 3). This ice flow pattern is also mirrored in the 1995–2015 ice flow directions which we used in our ice discharge calculations (Figures 6d and 6e). As for surging glaciers changes in ice flow direction over time are more likely to occur across slow ice flow areas where ice discharge is almost negligibly small anyway (Figure 6f), we expect the error resulting from our choice of a time-invariant ice flow direction pattern to be small. However, we acknowledge that this has introduced additional and unquantifiable uncertainty into the calculated ice discharge.

5. Results

5.1. Basin Extent and Grounding Lines

For basins 2 and 3 of FIIC we identified extents of 615.7 and 639.2 km^2, respectively when considering the 2018 grounding line as seaward basin boundary (Figure 1b). The lateral western boundary of the area covered by the two basins follows the ice flow trajectory that divides between ice flowing toward the sea within basin 2 and ice ending up at the land-terminating margin of FIIC further west. The southern boundary along the main ridge of the ice cap runs across the regions of minimal ice flow velocity, following along the line of diverging ice flow, that is, the ice divide. The lower section of the lateral northeastern boundary follows a prominent ridge-like terrain feature until reaching the main ice divide between the uppermost parts of basins 3 and 5. The lower part of the boundary between basins 2 and 3 runs along a series of spots of ice-free terrain previously identified in the RGI 6.0 ice cap outline. It continues to higher elevations across a region of minimal ice flow velocity following the line of converging ice flow. Even higher again, the inter-basin boundary follows the ice flow trajectory from the uppermost tip of ice flow convergence until the main ridge of the ice cap is reached.

We derived the grounding lines of the ice shelf in front of basins 2 and 3 for five individual years within the period 1993–2019 from Landsat images and for two additional years (2018 and 2021) from Sentinel-1 radar data (Figure 4). From the five Landsat images separate grounding lines were derived for the two basins. In basin 2, the delineation was complicated by unclear surface textures, which led to a discontinuous identification of the grounding line. From the two Sentinel-1 datasets, by contrast, we were able to identify one continuous grounding line per year. In both basins, our derived grounding line proxies share common characteristics of spatial distribution. Parts of them lie approximately perpendicular to the main flow directions of the glaciers and parts lie approximately parallel to them (cf. Figures 1b and 4i). Taken together, they clearly identify a curved grounding zone in both basins. Buoyancy calculations based on OIB data further supported the locations of the grounding zones in the central parts of the two basins (Figures 4h and 5).

We analyzed the variability of the grounding line locations over time and identified retreat in both basins (Figure 7). Over 1993–2019, the five Landsat images reveal overall grounding line retreats of 2.2 ± 1.3 km and 2.7 ± 0.9 km within a 1 km buffer region around the OIB flight tracks (cf. Figure 1a) in basins 2 and 3 respectively, which equals mean annual retreat rates of 0.086 ± 0.051 km a^{-1} in basin 2 and 0.106 ± 0.034 km a^{-1} in basin 3. Despite this overall retreat, we observed slight grounding line advances over 1993–1999 of 0.66 ± 1.15 km and 0.14 ± 1.02 km in basins 2 and 3, respectively (Figure 7). Afterward, a continuous but unequal grounding line retreat started in both basins. In basin 2, the advance was replaced by a slow retreat of 0.081 ± 0.038 km a^{-1} over 1999–2014, while in basin 3 distinctly larger retreat rates were observed over this period (0.175 ± 0.090 km a^{-1}). From 2014 onwards, the grounding line retreat increased considerably in basin 2, showing rates of 0.333 ± 0.152 km a^{-1} in 2014–2019. In basin 3, by contrast, retreat rates decreased to

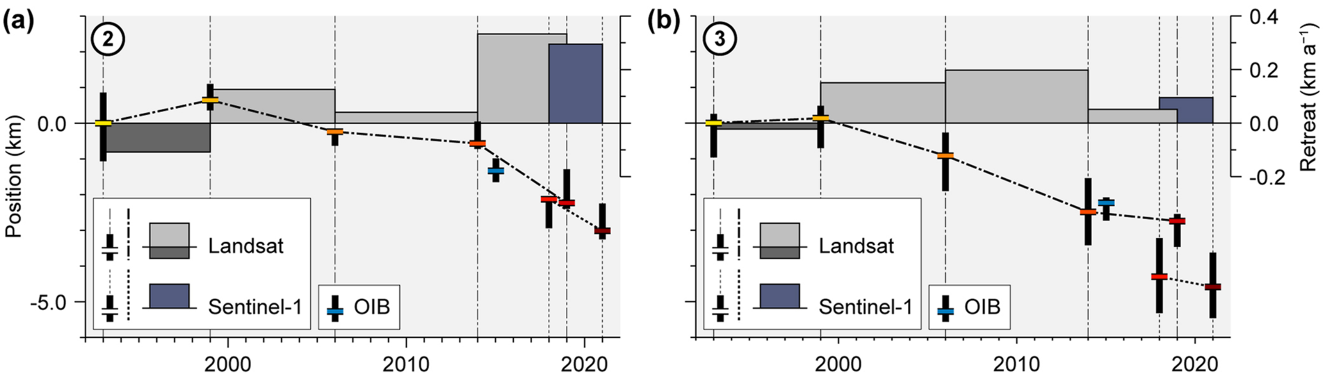

Figure 7. Temporal variability of the grounding line in basins 2 (a) and 3 (b) of Flade Isblink ice cap. Absolute grounding line positions (yearly colors analog to Figure 9) are shown relative to 1993 and were inferred along the Operation IceBridge (OIB) flight tracks (cf. Figure 1a). A negative grounding line position indicates retreat. The uncertainty ranges (thick black whiskers) represent spatial grounding line variability within a 1 km radius around the crossing points between grounding line and flight track. For each time interval between comparable grounding line proxies, the annual retreat rates are shown as box plot. A negative retreat rate indicates grounding line advance. Note that Landsat and Sentinel-1 based grounding lines are not directly comparable (cf. Section 3.3) and are thus treated separately here. The OIB derived 2015 grounding line positions are indicated by blue markers.

0.051 ± 0.243 km a^{-1} in 2014–2019. These 2014–2019 Landsat-based retreat rates are supported by Sentinel-1-based analyses over 2018–2021, which suggest similar retreat rates of 0.295 ± 0.258 km a^{-1} in basin 2 and 0.095 ± 0.595 km a^{-1} in basin 3.

Seaward of the grounding lines, we clearly identified a freely floating, shared ice shelf in front of basins 2 and 3, that shows only a few pinning points (Figure 4a). Assuming a glacier ice density of 875 kg m^{-3} (cf. Section 3.4) this ice shelf shows a mean thickness of 69.7 ± 25.5 m (mean ± one sigma) along the OIB flight tracks (Figure 5). Most of the pinning points are located in the transition region between the two basins, but a small one can also be found at the lateral northeastern boundary of the ice shelf in front of basin 3 (Figure 4). The grounded ice at the pinning points is only visible in the Sentinel-1 radar data (Figures 4f and 4h), but it is reasonable to assume that these points already existed prior to 2018 and form a permanent fixture of the ice shelf. On the Landsat images, the pinning points cannot be identified due to a lack of change in surface brightness. This lack can be explained by the limited extent of grounded ice and the hardly increased ice surface elevations in these areas. In addition to the pinning points, a central part of the outer ice shelf margin is grounded at the submarine slope of an elongated island that shelters the ice shelf from the open sea over a distance of almost 4 km (Figure 4a)

5.2. Flux Gates and Ice Discharge

The two curve-shaped flux gates that we defined landward of the ice shelf along the grounding lines have lengths of 14.5 km in basin 2 and 21.2 km in basin 3 (Figure 4a). Despite these considerably different lengths, the flux gate cross sections are much more similar and cover 1.19 km^2 in basin 2 and 1.31 km^2 in basin 3 (Figure 6). The difference in flux gate length is caused by the extensive section of thinner ice which forms the southwestern part of the flux gate in basin 3 (Figure 6). Accordingly, the main parts of the two cross sections show similar shapes with the subglacial troughs reaching down to −113 m a.s.l. in basin 2 and -121 m a.s.l. in basin 3.

The ice flow through these flux gates varied substantially over time with surges in both basins observed in 1996 and 2000/2001 (Figure 3). Accordingly, ice discharge from basins 2 and 3 was highly variable, too (Figure 8). For basin 2, Sentinel-1 velocities from 2020 yielded the minimum annual ice discharge (0.0091 ± 0.0090 Gt a^{-1}), while MEaSUREs InSAR velocities from 2000/2001 yielded the maximum (0.1827 ± 0.1545 Gt a^{-1}). For basin 3, ITS_LIVE velocities from 2014 yielded the minimum (0.0021 ± 0.0019 Gt a^{-1}) and MEaSUREs InSAR velocities from 2000/2001 yielded the maximum annual ice discharge (0.1202 ± 0.1009 Gt a^{-1}). For both basins, we identified three different, simultaneously occurring types of flow regimes (Figure 8). In the pre-surge period (1988–1992), basin 2 showed an annual ice discharge of 0.0438 ± 0.0047 Gt a^{-1} (mean ± one sigma), while basin 3 reached 0.0330 ± 0.0044 Gt a^{-1}. In basin 2, the mean annual ice discharge during the surge (1996–2001) was higher by a factor of 3.0 and reached 0.1454 ± 0.0528 Gt a^{-1}. In basin 3, the relative increase was even higher (factor of 3.6), with the mean annual ice discharge reaching 0.1192 ± 0.0014 Gt a^{-1} during the surge. From 2005

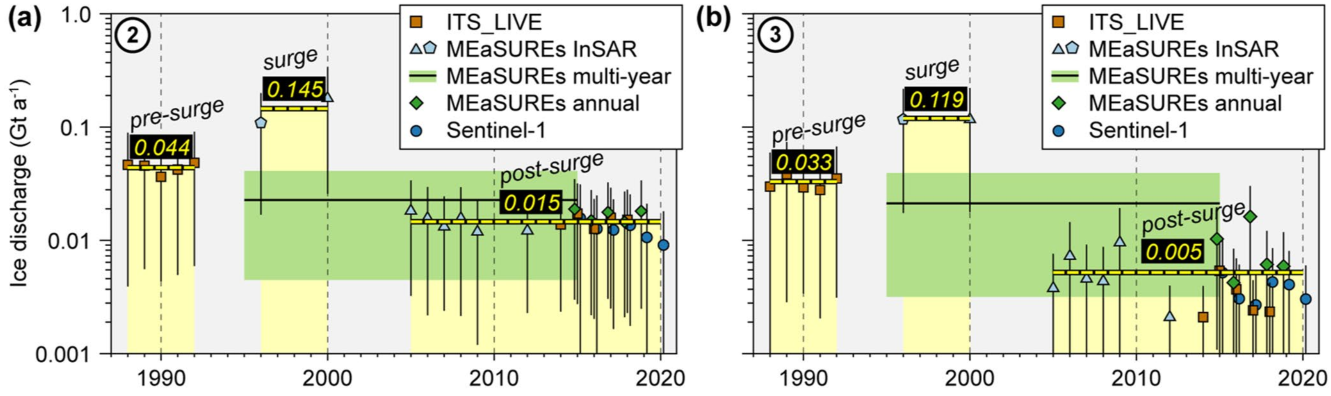

Figure 8. Ice discharge variability from basins 2 (a) and 3 (b) of Flade Isblink ice cap over time. Ice discharge (Equation 2) is displayed as annual rates with uncertainties (Equation 10) on the basis of different velocity datasets (cf. Figure 3). Periods before, during and after the surges in both basins are marked in yellow and with the respective mean annual ice discharge rates (Gt a^{-1}). Among the InSAR-based values (light blue symbols), the pentagon represents a value that is not based on MEaSUREs data, but on data derived from ERS Tandem phase InSAR observations (Palmer et al., 2010).

onwards, all data indicate a massive and persistent post-surge slowdown of ice discharge to mean annual rates of 0.0146 ± 0.0026 Gt a^{-1} (mean ± one sigma) in basin 2 and 0.0052 ± 0.0034 Gt a^{-1} in basin 3. This means, that ice discharge decreased by 90% after the surge in basin 2 and by 96% in basin 3. Simultaneous with this considerable reduction in ice supply, the extent of the ice shelf in front of the two basins reduced considerably from the pre-surge (Figure 4b) and surge period (Figure 4c) to the post-surge period (Figure 4d), while no significant further changes happened since 2006 (Figures 4d, 4e, and 4g).

Total ice discharge over the 1988-2020 study period amounts to 1.85 ± 1.59 Gt in basin 2 and 1.38 ± 1.22 Gt in basin 3, which is ∼25% less than from basin 2. We calculated these values from the mean annual ice discharge values of the pre-surge, surge and post-surge periods (Figure 8). These values represent most of the study period except for the years right before (1993–1995) and right after the surge (2002–2004). For these years without data, we assumed mean annual ice discharge values centered between the mean values of the respective preceding and succeeding periods.

5.3. Ice Flow Regime

The observed variability in ice flow regimes between pre-surge, surge and post-surge periods involved distinct changes, not only in ice flow velocity, but also in ice flow pattern. The different pattern across basins 2 and 3 are mainly characterized by changes in the locations of maximum ice flow velocity between the upper (>∼150 m a.s.l.) and steeper parts of the basin slopes and the lower (<∼150 m a.s.l.) and less steep parts.

In basin 3 during the pre-surge period, we observed the highest velocities across the upper NE slope, while during the surge the velocity maxima were located further downslope (Figures 3 and 9a). During the post-surge period, velocity maxima again occurred across the upper NE slope, but were slower and located at generally higher elevations than during the pre-surge period (Figure 9c). For the years during and shortly after the surge we also identified a deviating characteristic in the overall ice flow pattern of basin 3. During the surge, the main ice stream was fed by two different upstream branches, the main NE branch and an additional SW branch (Figure 3). The latter of these branches was not present before 1996 and gradually decelerated over the first half of the post-surge period until it became stagnant again in the 2012/2013 velocity pattern.

In basin 2, the evolution of the ice flow regime is similar in general, but the different patterns are less clear than in basin 3. Indeed, we found a slight decrease of elevation between the locations of the velocity maxima during the pre-surge and the surge period (Figure 9b). However, the clear re-increase of elevation after the surge, which we observed in basin 3, did not occur in basin 2. The locations of the velocity maxima of the post-surge period were scattered across a large range of terrain elevations. These elevations reached right down to the locations of the velocity maxima during the surge and they fully included the locations of the pre-surge period. Rather more striking for the evolution of the ice flow pattern in basin 2 is the occurrence of a persistent change in the origin of the main ice stream from the pre-surge toward the post-surge period (Figure 3). During the pre-surge period

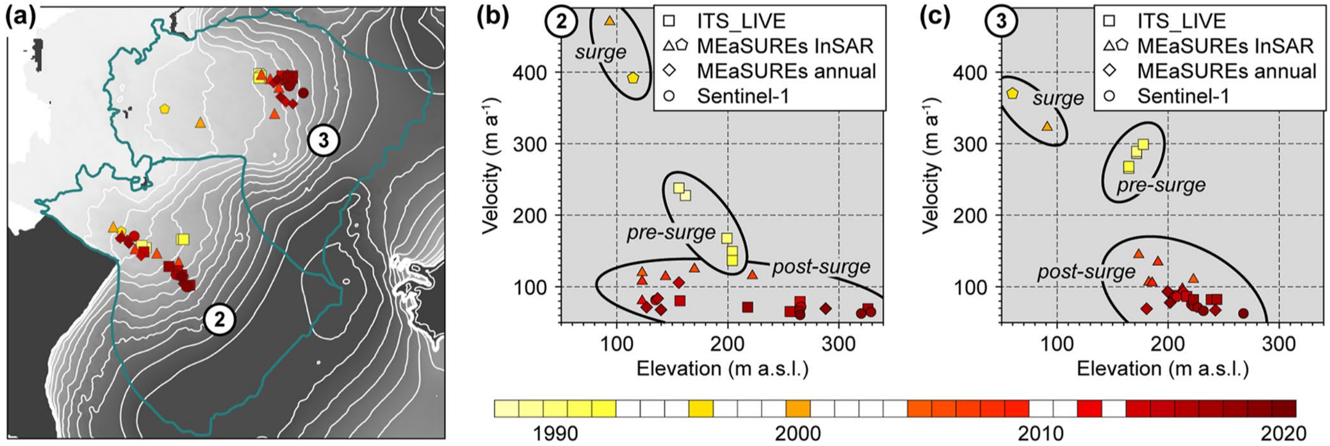

Figure 9. Temporal variability (color bar) of the locations of maximum annual surface ice flow velocities within basins 2 and 3 of Flade Isblink ice cap (a). For each data set and year, the relationship between surface elevation and ice flow velocity at the locations marked in (a) are shown for basin 2 (b) and basin 3 (c). Periods before, during and after the surges in both basins are indicated by black ellipses. Surface elevation contours in (a) show a spacing of 50 m. The basin boundaries are marked by turquoise lines and include the 2018 grounding line (cf. Figure 4f). Among the InSAR surface ice flow velocities, the pentagon represents a velocity that was not derived from the MEaSUREs data family, but from the velocity data set produced by Palmer et al. (2010).

the main ice stream of basin 2 was fed by one main eastern branch. During the surge, a second, equally strong central branch appeared in 1996 and until 2000/2001 even a third one, a western branch developed. Finally, over the first years of the post surge period, the initial eastern branch gradually decelerated until it became stagnant and completely disappeared in the 2007/2008 velocity pattern, leaving the central and western branches as sole sources of the main ice stream afterward. Accordingly, and following this shift in ice inflow, the pre-surge velocity maxima of basin 2 were located along the initial eastern branch, while the more high-lying post-surge velocity maxima were located in the central branch (Figure 9a).

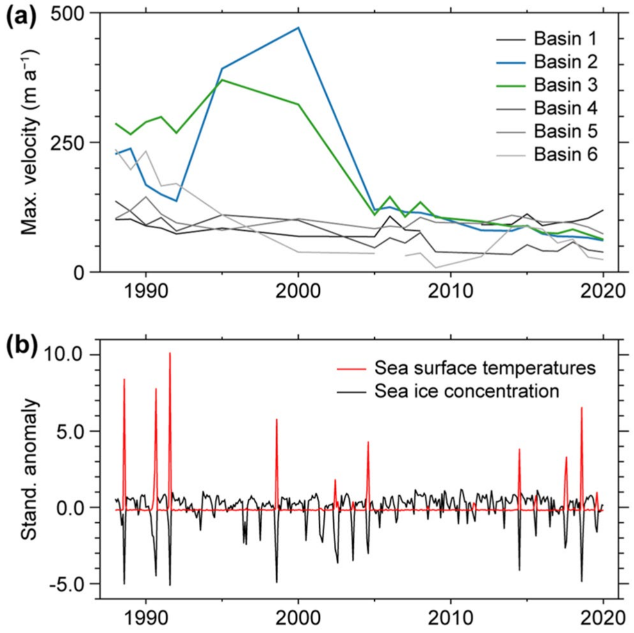

Figure 10. Variability of maximum ice flow velocity across the outlet basins (cf. Figure 1a) of Flade Isblink ice cap (a) and ocean conditions northwest of the ice cap (b) over the study period. For years where different velocity datasets were considered (cf. Figure 3), the displayed numbers in (a) represent the respective mean values. Ocean conditions in terms of ERA5 sea surface temperatures and sea ice concentration (Hersbach et al., 2020) are displayed as standardized monthly anomalies over the study period and represent means over a ~7,900 km^2 ocean region centered in front of basins 2 and 3 (cf. Figure S1 in the Supporting Information S1).

6. Discussion

6.1. Surge Dynamics

Our results reveal a substantial, rapid and persistent post-surge slowdown of ice discharge from basins 2 and 3 of FIIC. The surges happened simultaneously in both basins over at least 1996–2001 (Figure 8) but did not affect any of the other four basins of the ice cap (Figure 10a). In both basins they occurred in conjunction with a grounding line advance, which was observed over the period 1993–1999 (Figure 7). Further upstream, the surges followed a characteristic overall pattern (Figure 9): We found higher velocities occurred in the upper parts of the basins in the pre-surge period than in the post-surge period. For the pre-surge period, this suggests an ongoing accumulation of ice mass at higher elevations in the basins that was then transported down-glacier during the surge. Accordingly, in the surge period distinctly higher maximum ice flow velocities occurred closer to the grounding lines (Figure 9) and thus strongly support the occurrence of increased transport of ice mass to lower elevations. Moreover, a comparison of the ice flow velocity fields from the beginning of the surge (1996) and its end (2000/2001) revealed the development of additional branches of fast flowing ice in both basins over the surge period (Figure 3). This chronology suggests that the increase of ice flow during the surge was sufficient to "draw down" the upstream ice.

The described spatiotemporal pattern of the surges does not suggest a straightforward explanation regarding the underlying surge mechanism. In general, there are two different theories of glacier surges (Sevestre, 2015): the thermal switch mechanism which applies to cold-based or polythermal glaciers (Murray et al., 2003) and the hydrological switch mechanism which applies to temperate glaciers (Kamb et al., 1985). At first glance, the evidence we present for FIIC points to the former theory, that is, the “Svalbard-type”. This is supported by both Willis et al. (2015) and Cook (2016) who suggest FIIC is cold-based. A case study using the Elmer/Ice model (Gagliardini et al., 2013) revealed high longitudinal stress gradients close to the transition between fast flowing ice in basins 2 and 3 and more stagnant ice in the center of the ice cap during the surge (Cook, 2016). This suggests an increased ice flow was initiated across the whole lower parts of both basins. It is consistent with our observation of a “draw-down effect” on the upstream ice in basin 2 over the surge period and matches typical “Svalbard-type” characteristics (Murray et al., 2003). Also, the small differences of less than one order of magnitude in ice flow velocities between the quiescent phase and the surge phase, and the years-long duration of the surges are consistent with the “Svalbard-type” "mechanism (Murray et al., 2003).

However, there are contrary arguments. A typical “Svalbard-type” surge cycle shows a gradual velocity decrease over a years-long period from the surge to the post-surge quiescent phase, which takes much longer than the pre-surge speedup (Melvold & Hagen, 1998; Murray et al., 2003). At basins 2 and 3, the transition between surge and post-surge velocities appeared to be much faster (Figure 8). The modeling study of Cook (2016) found that additional input of water to the glacier bed was necessary to facilitate fast flow in basins 2 and 3 via cryo-hydrologic warming (Phillips et al., 2010), a process that develops from the standard “Svalbard-type” mechanism (Dunse et al., 2015). Cook (2016) identified a surplus of surface meltwater as the most likely source for this additional water input. However, modeled surface mass balances of FIIC reveal below average summer melt over the surge period (Rinne et al., 2011), which makes this source unlikely. Additionally, the grounding line advances in both basins over the surge period (Figure 7) imply a thickening of the downstream ice. This also contradicts “Svalbard-type” surges whose speedups begin at the lower portion of glaciers causing subsequent dynamic thinning.

An alternative reason for the observed velocity increases at basins 2 and 3 due to an external forcing by changing ocean conditions does not seem plausible at first sight. Ocean conditions in terms of sea ice concentration and sea surface temperatures in front of NW FIIC were stable over the study period (Figure 10b) and do not provide any realistic trigger. No abnormally long or frequent open water episodes, which would have had the potential to increase submarine melting at the ice shelf in front of basins 2 and 3 (Bendtsen et al., 2017), were present before or during the surge period. Beyond that, the increased submarine melting during such episodes would have resulted in a reduction of the buttressing effect of the ice shelf, a subsequent increase in downstream ice flow velocity and thus ice thinning and a grounding line retreat (Krug et al., 2015), contrary to what we observed in basins 2 and 3 (Figure 7). However, influences of a potential subsurface ocean warming on the ice shelf and the grounding lines and thus on ice flow within the two basins cannot be ruled out completely. Such a warming due to Atlantic water intrusions into deeper coastal waters around Greenland has been documented for recent decades and also occurred in the northeastern sector of the island (Wood et al., 2021). It was not investigated here, but could potentially have played a role in the ice shelf's dynamics by inducing an intensified melting at the ice shelf's grounding line, leading to a short-term acceleration of ice flow.

To overcome this context of conflicting evidence we here propose a modifying role of the ice shelf on the morpho-topographic appearance of the “Svalbard-type” surges in basins 2 and 3. We suggest that the buttressing effect of the ice shelf with respect to the grounded upstream ice in the two basins was strong enough to partly restrict ice discharge, which led to an increase in ice thickness and a subsequent advance of the grounding line. This helps to explain the inverted temporal evolution of ice flow velocity in basins 2 and 3 (Figure 10a) compared to an ideal “Svalbard-type” surge. First, the buttressing effect of the ice shelf buffered the usually rapid acceleration in the pre-surge period. Maximum ice flow velocities were already high over the entire pre-surge period (Figure 10a), indicating a gradual increase of ice flow. Second, the buttressing effect enhanced the usually gradual deceleration toward the post-surge period, leading to the much more rapid post-surge slowdown observed.

This explanation does not address the issue described above relating to insufficient surface meltwater required for the cryo-hydrologic warming processes suggested by Cook (2016). A previous study showed that in autumn 2011 a subglacial lake under the central southwestern parts of FIIC drained abruptly, creating a large ice cauldron in the uppermost parts of basin 1 (Willis et al., 2015). This event shows that alternative explanations exist for substantial, short-term changes in the ice cap's hydrology, which could significantly alter ice dynamics (e.g., Das et al., 2008). Such subglacial lake drainages have also been documented for the Greenland ice sheet (Palmer et al., 2015). However, there are no indications that such a process might have played a role in the surges of basins 2 and 3 described here.

After the surge, the ice flow in basin 3 returned to its original, pre-surge pattern, while a permanent change seemed to be initiated by the "draw-down effect" that occurred during the surge in basin 2. In the post-surge period, the main ice flow line in this basin was focused on the newly developed, central and western branches while the eastern branch became "deactivated" (Figure 3). Moreover, the location of maximum ice flow velocity returned to higher elevations in the post-surge period (Figure 9). This not only happened in basin 2, but also in basin 3, and is therefore consistent with thickening in the upper parts of both basins that was observed over 2004–2008 (Rinne et al., 2011). The thickening in basins 2 and 3 continued in 2010–2017 with maximum rates in basin 3 occurring slightly downstream of the locations of maximum ice flow velocity during this period (cf. Figure 9a) (Kappelsberger et al., 2021). This coincidence suggests a long-lasting dynamic recovery from the surge-induced, basin-wide ice mass losses, as has been observed previously at other glaciers in Greenland (Hill et al., 2017).

6.2. Ice-Shelf and Grounding-Line Stability

While the ice was thickening in the upper parts of basins 2 and 3 during much of the post-surge period, a thinning was evident across the lower parts (Kappelsberger et al., 2021; Rinne et al., 2011). Coincident to these ice thickness fluctuations, the grounding line advanced in both basins during the surge (Figure 7) while a continuous retreat occurred afterward. This retreat occurred seaward from the respective deepest points of the submarine troughs in both basins (Figure 4) and thus over low gradient retrograde sloping parts of the beds (cf. Figure 5). The resulting increase in the buoyancy forces suggests a positive-feedback response in both basins implying dynamic instability (e.g., Oerlemans & Nick, 2005; Schoof, 2007). However, buttressing forces of the shared ice shelf in front of basins 2 and 3 oppose the increasing buoyancy forces and act as a stabilizing effect (Haseloff & Sergienko, 2018; Pegler, 2018). The balance between these forces is different in the two basins though, as can be inferred from the differing of the grounding line migration rates with time (Figure 7). In basin 3 the grounding line retreat rates decreased after 2014, while concurrently a marked increase occurred in basin 2 (Figure 7). As the increase of the buoyancy forces during grounding line retreat can be deemed similar in both basins due to similar bed slopes (cf. Figure 5), this difference strongly suggests varied buttressing forces.

The ice shelf outer margins have been rather stable in both basins since 2006, but a considerable reduction of sea ice is visible in the Landsat images from summer 2014 and 2019 compared to the situation in summer 2006 (Figure 4). This fact is also mirrored in sea ice concentrations around the ice shelf, which show distinctly negative summer anomalies from 2014 onwards compared to preceding years (Figure 10b). However, sea ice coverage exerts a buttressing force on calving fronts, that is, it stabilizes the edges of the ice shelf (e.g., Amundson et al., 2010; Robel, 2017). And these edges, in turn, are dynamically linked to the grounding line locations via ice shelf length and the related buttressing forces (Haseloff & Sergienko, 2018). As in front of basin 3 the ice shelf is confined by an island and by a pinning point at its lateral margin (Figure 4a), the impact of sea ice reduction on the grounding line is suggested to be more severe in front of basin 2 where no lateral confinement of the ice shelf exists. This finally led to the different behavior of the grounding lines in the two basins from 2014 onwards.

In basin 3, the balance of buoyancy and buttressing forces shifted with time in favor of the latter. With a stable and partly confined outer ice shelf margin the grounding line retreat implied an ice shelf extension and thus an increase of the buttressing forces (Pegler, 2018). Moreover, the grounding line approached the deepest part of the submarine trough toward the end of the study period (Figures 4a and 5). This implied decreasing slope angles of the retrograde bed and a slower increase of buoyancy forces with time. In combination, these two effects together with the rather constant ice discharge during the post-surge period (Figure 8b) allow for the observed slowdown of grounding line retreat in basin 3 after 2014 (Figure 7b).

In basin 2, the balance of forces developed differently. The increase of buttressing forces due to the occurring grounding line retreat and the implied ice shelf extension was limited by the discontinuation of the ice shelf confinement by summer sea ice coverage from 2014 onwards. This resulted in weaker ice shelf margins. Given the still (albeit slower, similar to basin 3) increasing buoyancy forces and the rather constant ice discharge

(Figure 8a), the shift of forces in favor of buoyancy allowed for the observed acceleration of grounding line retreat in basin 2 after 2014 (Figure 7a).

Even more as in recent years, the future of the grounding line retreat in basins 2 and 3 of FIIC and thus of the overall stability of these ice cap basins will be controlled by the state of the shared ice shelf. With further retreat the grounding lines will approach the prograde-sloping, rear parts of the submarine troughs (Figure 5). This will lead to decreasing buoyancy forces, a shift of the balance of forces in favor of ice shelf buttressing and ultimately a stable grounding line position (Pegler, 2018). However, on smooth (compared to ice thickness) subglacial topographies (as in basins 2 and 3) unstable grounding line positions may also occur on prograde-sloping beds, depending on the strength of the buttressing forces (Pegler, 2018; Sergienko & Wingham, 2021). This implies that a persistence of ice shelf buttressing may be vital for basin stability and that any reduction of the ice shelf extent may result in a resumed grounding line retreat. However, this continued existence of the ice shelf is not guaranteed.

In basin 3, both the advance and the overall retreat of the grounding line were concentrated in those parts of the trough (Figure 4) that are deepest, and show the thickest ice according to BM3 bed elevations (Figures 2b and 6). In contrast, grounding line migration in the region of higher BM3 bed elevations, and thus thinner ice, across the southwestern part of the flux gate (Figures 2b and 6) was minimal. This finding suggests that future ice thinning combined with further grounding line retreat might lead to a separation of the continuous ice cover of basins 2 and 3 in the afore-mentioned region of higher BM3 bed elevations. Such a separation might also have severe implications for the existence of the ice shelf.

At present, the ice shelf is almost continuously floating downstream of the grounding lines in basins 2 and 3 and only has few pinning points (Figure 4a). This finding confirms previous assumptions that were based on the presence of a continuous undulating surface that has long been visible on aerial photography (Higgins, 1991; Koenig et al., 1952). Our analyses suggest an ice shelf thickness of 69.7 ± 25.5 m (mean ± one sigma), which agrees within uncertainty with the thickness of ~45 m which has been suggested by Bendtsen et al. (2017) for the ice shelf in front of basin 2 based on sea water salinity data. At present, the mass gain of the ice shelf by ice discharge from basins 2 and 3 roughly balances out with mass loss due to marine melting (Bendtsen et al., 2017), so a reduction in upstream ice supply due to a separation of the grounded ice of basins 2 and 3, as described above, would destabilize the ice shelf and could have the potential to even put it at risk of disintegration.

A potential future reduction of sea ice concentration and a related warming of ocean waters in front of NW FIIC would further accelerate this destabilization as marine melt rates could increase substantially. Such an increase could weaken the outer margins of the ice shelf, especially in areas where no pinning points exist to support stability. Hence, the southwestern part of the ice shelf (in front of basin 2) is more at risk of disintegration than the northeastern part (in front of basin 3) whose outer margins are grounded sporadically (Figure 4a). An increase of marine melt rates would thus lead to a reduction of the ice shelf buttressing effect fostering a continued grounding line retreat and an increase of ice flow in basin 2 and later also in basin 3 (Haseloff & Sergienko, 2018; Krug et al., 2015). Therefore, ice discharge – which has been substantially reduced in the post-surge period (Figure 8) – might return to the higher levels observed at the end of the 20th Century as a result of future climate warming.

6.3. Arctic-Wide Perspective

During our study period 1988–2020, the mean rate of ice discharge to the ocean from NW FIIC was small (0.10 ± 0.08 km^3 a^{-1} for both basins) compared to other Arctic ice caps. In the Canadian Arctic, ice discharges of 0.53 km^3 a^{-1} and 0.67 km^3 a^{-1} have been reported for Devon Ice Cap and Agassiz Ice Cap (Burgess et al., 2005; Williamson et al., 2008). These values are roughly five to seven times higher than what we found for basins 2 and 3 in this study, despite Devon and Agassiz Ice Caps being only about twice as large as the entire FIIC. However, the differences in ice cap-wide annual ice discharge might be smaller than they first appear, as it is reasonable to expect that FIIC also loses substantial mass by ice discharge from its other four marine-terminating outlet basins (Figure 1a).

The evolution of peak ice flow velocities in the six outlet basins suggests distinctly slower, but steady ice flow outside of basins 2 and 3 (Figure 10a). Nevertheless, even during the surge period, the ice flow velocities in basins 2 and 3 were orders of magnitude smaller than what has been reported previously from surging basins at other

Arctic ice caps, such as basin 3 of Austfonna ice cap, Svalbard, which showed velocities of up to 18.8 m day^{-1} (Dunse et al., 2015) compared to just 1.3 m day^{-1} at basin 2 of FIIC. The surges in basins 2 and 3 were thus of rather low intensity.

Taken together, these comparisons reveal that the ice discharge from basins 2 and 3 of FIIC during the period 1988–2020 was small when considering the Arctic-wide perspective. However, it matches the order of magnitude that could be expected from close to zero overall ice mass changes and slightly positive surface mass balances that had been reported by Rinne et al. (2011).

7. Conclusions

We carried out the first grounding line mapping at the outlet basins 2 and 3 of Flade Isblink ice cap (Figure 1) and performed a detailed analysis of grounding line migration over the period 1993–2021. In addition, we carried out the first quantification of ice discharge and its variability from the two basins over the slightly longer period 1988–2020. Based on these analyses we discussed and explained potential mechanisms behind the surges that occurred simultaneously in both basins over at least 1996–2001.

The grounding lines in basins 2 and 3 advanced slightly between 1993 and 1999 during surges of both glaciers, before starting a continuous retreat (Figure 7). Overall, we found grounding line retreats of 2.2 ± 1.3 km in basin 2 and 2.7 ± 0.9 km in basin 3, when comparing the positions in 2019 to the initial positions in 1993. During the entire study period, the grounding line migration in both basins occurred over retrograde sloping parts of deep submarine troughs. This implied constantly increasing water depths and buoyancy forces during retreat, which fostered a positive-feedback response. However, opposing these buoyancy forces the spatially varying buttressing effect of the shared ice shelf in front of basins 2 and 3 led to a differing balance of forces at the grounding lines of these basins and thus to differing retreat rates.

We calculated total ice discharges over the period 1988–2020 of 1.85 ± 1.59 Gt in basin 2 and 1.38 ± 1.22 Gt in basin 3 and revealed a large variability in annual rates (Figure 8). During the period 1996–2001 the surges in both basins led to maximum ice flow velocities reaching almost 500 m a^{-1} in basin 2 and more than 300 m a^{-1} in basin 3 (Figure 9). After the surge, we observed very large ice flow decelerations that have persisted until the present day. In basin 2, this slowdown led to a decrease of mean annual ice discharge rates to just ~10% (0.015 ± 0.003 Gt a^{-1}) when compared to the surge level (0.145 ± 0.053 Gt a^{-1}). In basin 3, the slowdown was even more pronounced. During the post-surge period (i.e., after 2001) ice flow all but stagnated, with mean annual rates of ice discharge from this basin reducing to ~4% (0.005 ± 0.003 Gt a^{-1}) of the discharge rate during the surge (0.119 ± 0.001 Gt a^{-1}).

The combined picture of grounding line migration and ice flow evolution over the study period suggest "Svalbard-type" surges in both basins that were modified by buttressing effects of the downstream ice shelf. This buttressing effects led to atypical increases of ice thickness across the lowermost parts of the glacier which resulted in a grounding line advance over the surge period. A still missing link in the explanation of the surges in basins 2 and 3 of Flade Isblink ice cap is the water required for surge initiation. SMB data does not support melt water quantities essential for velocity increase. More research is necessary to identify the direct trigger mechanisms responsible for the surging velocities and increased ice discharges.

Potential future reduction of sea ice coverage around NW Flade Isblink ice cap and increases of ocean temperatures during the resulting open water episodes might lead to a thinning and shrinking of the shared ice shelf in front of basins 2 and 3 and thus to a reduction of its buttressing effect. The persistence of this ice shelf under the influence of potential future ocean warming may thus be vital for grounding line and subsequent basin stability.

Data Availability Statement

The Landsat data used in this study are available from the United States Geological Survey (USGS) Earth Explorer website subject to registration. The PANGAEA earth science data repository provides access to the Sentinel-1 ice flow velocity data (https://doi.org/10.1594/PANGAEA.935651) and the Sentinel-1 radar double-difference interferograms (https://doi.org/10.1594/PANGAEA.935652).

Acknowledgments

This study was funded by the German Federal Ministry of Education and Research (BMBF) via grants no. 03F0778D and 03F0855B. Additional funding was provided via grant no. 03F0855D (BMBF) and grant no. MA 6966/6-1 of the German Research Foundation (DFG). Open access funding enabled and organized by Projekt DEAL.

References

Amundson, J. M., Fahnestock, M., Truffer, M., Brown, J., Lüthi, M. P., & Motyka, R. J. (2010). Ice mélange dynamics and implications for terminus stability, Jakobshavn Isbræ, Greenland. *Journal of Geophysical Research*, *115*, F01005. https://doi.org/10.1029/2009JF001405

Bendtsen, J., Mortensen, J., Lennert, K., Ehn, J. K., Boone, W., Galindo, V., et al. (2017). Sea ice breakup and marine melt of a retreating tidewater outlet glacier in northeast Greenland (81°N). *Scientific Reports*, *7*, 2045–2322. https://doi.org/10.1038/s41598-017-05089-3

Bevis, M., Harig, C., Khan, S. A., Brown, A., Simons, F. J., Willis, M., et al. (2019). Accelerating changes in ice mass within Greenland, and the ice sheet's sensitivity to atmospheric forcing. *Proceedings of the National Academy of Sciences of the United States of America*, *116*, 1934–1939. https://doi.org/10.1073/pnas.1806562116

Bindschadler, R. A., Choi, H., Wichlacz, A., Bingham, R., Bohlander, J., Brunt, K., et al. (2011). Getting around Antarctica: New high-resolution mappings of the grounded and freely floating boundaries of the Antarctic ice sheet created for the international polar year. *The Cryosphere*, *5*(3), 569–588. https://doi.org/10.5194/tc-5-569-2011

Bolch, T., Sandberg Sørensen, L., Simonsen, S. B., Mölg, N., Machguth, H., Rastner, P., & Paul, F. (2013). Mass loss of Greenland's glaciers and ice caps 2003–2008 revealed from ICESat data. *Geophysical Research Letters*, *40*, 875–881. https://doi.org/10.1002/grl.50270

Brunt, K., Fricker, H. A., Padman, L., Scambos, T., & O'Neel, S. (2010). Mapping the grounding zone of the Ross Ice Shelf, Antarctica, using ICESat laser altimetry. *Annals of Glaciology*, *51*(55), 71–79. https://doi.org/10.3189/172756410791392790

Burgess, D. O., Sharp, M., Mair, D. W. F., Dowdeswell, J. A., & Benham, T. J. (2005). Flow dynamics and iceberg calving rates of the Devon ice cap, Nunavut, Canada. *Journal of Glaciology*, *51*, 219–230. https://doi.org/10.3189/172756505781829430

Christie, F. D. W., Bingham, R. G., Gourmelen, N., Tett, S. F. B., & Muto, A. (2016). Four-decade record of pervasive grounding line retreat along the Bellingshausen margin of West Antarctica. *Geophysical Research Letters*, *43*(11), 5741–5749. https://doi.org/10.1002/2016GL068972

Cogley, J. G., Hock, R., Rasmussen, L. A., Arendt, A. A., Bauder, A., Braithwaite, R. J., et al. (2011). Glossary of glacier mass balance and related terms. *IHP-VII technical documents in hydrology No. 86, IACS contribution No. 2*. UNESCO-IHP.

Cook, S. (2016). *Blink and you'll miss it: An investigation into surging on Flade Isblink, Greenland*. M.Ph. thesis, University of Cambridge.

Cuffey, K., & Paterson, W. S. B. (2010). *The physics of glaciers* (4th ed.). Academic Press

Das, S. B., Joughin, I., Behn, M. D., Howat, I. M., King, M. A., Lizarralde, D., & Bhatia, M. P. (2008). Fracture propagation to the base of the Greenland ice sheet during Supraglacial lake drainage. *Science*, *320*, 778–781. https://doi.org/10.1126/science.1153360

Dunse, T., Schellenberger, T., Hagen, J. O., Kääb, A., Schuler, T. V., & Reijmer, C. H. (2015). Glacier-surge mechanisms promoted by a hydro-thermodynamic feedback to summer melt. *The Cryosphere*, *9*, 197–215. https://doi.org/10.5194/tc-9-197-2015

Enderlin, E. M., Howat, I. M., Jeong, S., Noh, M.-J., van Angelen, J. H., & van den Broeke, M. R. (2014). An improved mass budget for the Greenland ice sheet. *Geophysical Research Letters*, *41*, 866–872. https://doi.org/10.1002/2013GL059010

Friedl, P., Seehaus, T., & Braun, M. (2021). Global time series and temporal mosaics of glacier surface velocities derived from Sentinel-1 data. *Earth System Science Data*, *13*, 4653–4675. https://doi.org/10.5194/essd-13-4653-2021

Friedl, P., Seehaus, T. C., Wendt, A., Braun, M. H., & Höppner, K. (2018). Recent dynamic changes on Fleming glacier after the disintegration of wordie ice shelf, Antarctic Peninsula. *The Cryosphere*, *12*, 1347–1365. https://doi.org/10.5194/tc-12-1347-2018

Friedl, P., Weiser, F., Fluhrer, A., & Braun, M. H. (2020). Remote sensing of glacier and ice sheet grounding lines: A review. *Earth-Science Reviews*, *201*, 102948. https://doi.org/10.1016/j.earscirev.2019.102948

Gagliardini, O., Zwinger, T., Gillet-Chaulet, F., Durand, G., Favier, L., de Fleurian, B., et al. (2013). Capabilities and performance of Elmer/Ice, a new-generation ice sheet model. *Geoscientific Model Development*, *6*, 1299–1318. https://doi.org/10.5194/gmd-6-1299-2013

Gardner, A. S., Fahnestock, M. A., & Scambos, T. A. (2019). *ITS_LIVE regional glacier and ice sheet surface velocities*. Data archived at National Snow and Ice Data Center. https://doi.org/10.5067/6II6VW8LLWJ7

Gardner, A. S., Moholdt, G., Scambos, T., Fahnstock, M., Ligtenberg, S., van den Broeke, M., & Nilsson, J. (2018). Increased West Antarctic and unchanged East Antarctic ice discharge over the last 7 years. *The Cryosphere*, *12*(2), 521–547. https://doi.org/10.5194/tc-12-521-2018

Haseloff, M., & Sergienko, O. V. (2018). The effect of buttressing on grounding line dynamics. *Journal of Glaciology*, *64*(245), 417–431. https://doi.org/10.1017/jog.2018.30

Helk, J. V., & Dunbar, M. (1953). Ice islands: Evidence from north Greenland. *Arctic*, *6*(4), 263–271. https://doi.org/10.14430/arctic3881

Hersbach, H., Bell, B., Berrisford, P., Hirahara, S., Horányi, A., Muñoz-Sabater, J., et al. (2020). The ERA5 global reanalysis. *Quarterly Journal of the Royal Meteorological Society*, *146*(739), 1999–2049. https://doi.org/10.1002/qj.3803

Higgins, A. K. (1991). North Greenland glacier velocities and calf ice production. *Polarforschung*, *60*(1), 1–23.

Hill, E. A., Carr, J. R., & Stokes, C. R. (2017). A review of recent changes in major marine-terminating outlet glaciers in northern Greenland. *Frontiers in Earth Science*, *4*, 111. https://doi.org/10.3389/feart.2016.00111

Howat, I., Negrete, A., & Smith, B. (2014). The Greenland Ice Mapping Project (GIMP) land classification and surface elevation data sets. *The Cryosphere*, *8*, 1509–1518. https://doi.org/10.5194/tc-8-1509-2014

Hugonnet, R., McNabb, R., Berthier, E., Menounos, B., Nuth, C., Girod, L., et al. (2021). Accelerated global glacier mass loss in the early twenty-first century. *Nature*, *592*, 726–731. https://doi.org/10.1038/s41586-021-03436-z

Joughin, I. (2010). Greenland flow variability from ice-sheet-wide velocity mapping. *Journal of Glaciology*, *56*(197), 415–430. https://doi.org/10.3189/002214310792447734

Joughin, I. (2020). *MEaSUREs Greenland annual ice sheet velocity mosaics from SAR and Landsat, version 2. Boulder, Colorado USA*. NASA National Snow and Ice Data Center Distributed Active Archive Center. https://doi.org/10.5067/TZZDYD94IMJB

Joughin, I., Smith, B., Howat, I., & Scambos, T. (2015). *MEaSUREs Greenland ice sheet velocity Map from InSAR data, version 2*. NASA National Snow and Ice Data Center Distributed Active Archive Center. https://doi.org/10.5067/OC7B04ZM9G6Q

Joughin, I., Smith, B., Howat, I., & Scambos, T. (2016). *MEaSUREs multi-year Greenland ice sheet velocity mosaic, version 1*, NASA national snow and ice data center distributed active archive center. https://doi.org/10.5067/QUA5Q9SVMSJG

Joughin, I., Smith, B. E., & Howat, I. M. (2018). A complete map of Greenland ice velocity derived from satellite data collected over 20 years. *Journal of Glaciology*, *64*, 1–11. https://doi.org/10.1017/jog.2017.73

Joughin, I., Smith, B. E., Howat, I. M., Scambos, T., & Moon, T. (2010). Greenland flow variability from ice-sheet-wide velocity mapping. *Journal of Glaciology*, *56*, 415–430. https://doi.org/10.3189/002214310792447734

Kamb, B., Raymond, C. F., Harrison, W. D., Engelhardt, H., Echelmeyer, K. A., Humphrey, N., et al. (1985). Glacier surge mechanism: 1982-1983 surge of the variegated glacier, Alaska. *Science*, *227*(4686), 469–479. https://doi.org/10.1126/science.227.4686.469

Kappelsberger, M. T., Strößenreuther, U., Scheinert, M., Horwath, M., Groh, A., Knöfel, C., et al. (2021). Modeled and observed bedrock displacements in north-east Greenland using refined estimates of presentday ice-mass changes and densified GNSS measurements. *Journal of Geophysical Research: Earth Surface*, *126*, e2020JF005860. https://doi.org/10.1029/2020JF005860

King, M. D., Howat, I. M., Jeong, S., Noh, M. J., Wouters, B., Noël, B., & van den Broeke, M. R. (2018). Seasonal to decadal variability in ice discharge from the Greenland Ice Sheet. *The Cryosphere*, *12*, 3813–3825. https://doi.org/10.5194/tc-12-3813-2018

Koenig, L. S., Greenaway, K. R., Dunbar, M., & Hattersley-Smith, G. (1952). Arctic ice islands. *Arctic*, *5*(2), 67–103. https://doi.org/10.14430/arctic3901

Krabill, W., Abdalati, W., Frederick, E., Manizade, S., Martin, C., Sonntag, J., et al. (2000). Greenland Ice Sheet: High-elevation balance and peripheral thinning. *Science*, *289*, 428–430. https://doi.org/10.1126/science.289.5478.428

Krabill, W., Abdalati, W., Frederick, E., Manizade, S., Martin, C., Sonntag, J., et al. (2002). Aircraft laser altimetry measurement of elevation changes of the Greenland ice sheet: Technique and accuracy assessment. *Journal of Geodynamics*, *34*, 357–376. https://doi.org/10.1016/S0264-3707(02)00040-6

Krieger, L., Floricioiu, D., & Neckel, N. (2020). Drainage basin delineation for outlet glaciers of Northeast Greenland based on Sentinel-1 ice velocities and TanDEM-X elevations. *Remote Sensing of Environment*, *237*, 111483. https://doi.org/10.1016/j.rse.2019.111483

Krieger, L., Johnson, E., & Floricioiu, D. (2020). A new drainage basin delineation for the Southern Patagonian Ice Field based on TerraSAR-X velocities and TanDEM-X elevations. *IEEE Latin American GRSS & ISPRS Remote Sensing Conference (LAGIRS)*, 441–444. https://doi.org/10.1109/LAGIRS48042.2020.9165646

Krug, J., Durand, G., Gagliardini, O., & Weiss, J. (2015). Modelling the impact of submarine frontal melting and ice mélange on glacier dynamics. *The Cryosphere*, *9*, 989–1003. https://doi.org/10.5194/tc-9-989-2015

Le Meur, E., Sacchettini, M., Garambois, S., Berthier, E., Drouet, A. S., Durand, G., et al. (2014). Two independent methods for mapping the grounding line of an outlet glacier – An example from the Astrolabe Glacier, Terre Adélie, Antarctica. *The Cryosphere*, *8*(4), 1331–1346. https://doi.org/10.5194/tc-8-1331-2014

Lenaerts, J. T. M., Camron, M. D., Wyburn-Powell, C. R., & Kay, J. E. (2020). Present-day and future Greenland ice sheet precipitation frequency from CloudSat observations and the community Earth system model. *The Cryosphere*, *14*, 2253–2265. https://doi.org/10.5194/tc-14-2253-2020

Li, J., Paden, J., Leuschen, C., Rodriguez-Morales, F., Hale, R. D., Arnold, E. J., et al. (2013). High-altitude radar measurements of ice thickness over the Antarctic and Greenland ice sheets as part of operation IceBridge. *IEEE Transactions on Geoscience and Remote Sensing*, *51*, 742–754. https://doi.org/10.1109/TGRS.2012.2203822

Lüttig, C., Neckel, N., & Humbert, A. (2017). A combined approach for filtering ice surface velocity fields derived from remote sensing methods. *Remote Sensing*, *9*, 1062. https://doi.org/10.3390/rs9101062

Machguth, H., Rastner, P., Bolch, T., Mölg, N., Sandberg Sørensen, L., Aðalgeirsdottir, G., et al. (2013). The future sea-level rise contribution of Greenland's glaciers and ice caps. *Environmental Research Letters*, *8*, 025005. https://doi.org/10.1088/1748-9326/8/2/025005

Mankoff, K. D., Solgaard, A., Colgan, W., Ahlstrøm, A. P., Khan, S. A., & Fausto, R. S. (2020). Greenland Ice Sheet solid ice discharge from 1986 through March 2020. *Earth System Science Data*, *12*, 1367–1383. https://doi.org/10.5194/essd-12-1367-2020

Melvold, K., & Hagen, J. O. (1998). Evolution of a surge-type glacier in its quiescent phase: Kongsvegen, Spitsbergen, 1964–95. *Journal of Glaciology*, *44*(147), 394–404. https://doi.org/10.3189/S0022143000002720

Moholdt, G., Wouters, B., & Gardner, A. S. (2012). Recent mass changes of glaciers in the Russian High Arctic. *Geophysical Research Letters*, *39*, L10502. https://doi.org/10.1029/2012GL051466

Möller, M., Finkelnburg, R., Braun, M., Scherer, D., & Schneider, C. (2013). Variability of the climatic mass balance of Vestfonna ice cap, northeastern Svalbard, 1979-2011. *Annals of Glaciology*, *54*(63), 254–264. https://doi.org/10.3189/2013AoG63A407

Möller, M., & Kohler, J. (2018). Differing climatic mass balance evolution across Svalbard glacier regions over 1900–2010. *Frontiers in Earth Science*, *6*, 128. https://doi.org/10.3389/feart.2018.00128

Möller, M., & Schneider, C. (2010). Volume change at gran campo Nevado, Patagonia, 1984–2000: A reassessment based on new findings. *Journal of Glaciology*, *56*(196), 363–365. https://doi.org/10.3189/002214310791968458

Möller, M., & Schneider, C. (2015). Temporal constraints on future accumulation-area loss of a major Arctic ice cap due to climate change (Vestfonna, Svalbard). *Scientific Reports*, *5*, 8079. https://doi.org/10.1038/srep08079

Morlighem, M., Williams, C. N., Rignot, E., An, L., Arndt, J. E., Bamber, J. L., et al. (2017a). *IceBridge BedMachine Greenland, version 3*. NASA National Snow and Ice Data Center Distributed Active Archive Center. https://doi.org/10.5067/2CIX82HUV88Y

Morlighem, M., Williams, C. N., Rignot, E., An, L., Arndt, J. E., Bamber, J. L., et al. (2017b). BedMachine v3: Complete bed topography and ocean bathymetry mapping of Greenland from multibeam echo sounding combined with mass conservation. *Geophysical Research Letters*, *44*, 11051–11061. https://doi.org/10.1002/2017GL074954

Mouginot, J., Rignot, E., Bjørk, A. A., van den Broeke, M., Millan, R., Morlighem, M., et al. (2019). Forty-six years of Greenland Ice Sheet mass balance from 1972 to 2018. *Proceedings of the National Academy of Sciences*, *116*, 9239–9244. https://doi.org/10.1073/pnas.1904242116

Mouginot, J., Rignot, E., Scheuchl, B., Fenty, I., Khazendar, A., Morlighem, M., et al. (2015). Fast retreat of zachariæ isstrøm, northeast Greenland. *Science*, *350*, 1357–1361. https://doi.org/10.1126/science.aac7111

Mouginot, J., Rignot, E., Scheuchl, B., & Millan, R. (2017). Comprehensive annual ice sheet velocity mapping using Landsat-8, Sentinel-1, and RADARSAT-2 data. *Remote Sensing*, *9*(4), 364. https://doi.org/10.3390/rs9040364

Murray, T., Strozzi, T., Luckman, A., Jiskoot, H., & Christakos, P. (2003). Is there a single surge mechanism? Contrasts in dynamics between glacier surges in Svalbard and other regions. *Journal of Geophysical Research*, *108*(B5). https://doi.org/10.1029/2002JB001906

Noël, B., van de Berg, W. J., Lhermitte, S., & van den Broeke, M. R. (2019). Rapid ablation zone expansion amplifies north Greenland mass loss. *Science Advances*, *5*(9), eaaw0123. https://doi.org/10.1126/sciadv.aaw0123

Noël, B., van de Berg, W. J., Lhermitte, S., Wouters, B., Machguth, H., Howat, I., et al. (2017). A tipping point in refreezing accelerates mass loss of Greenland's glaciers and ice caps. *Nature Communications*, *8*, 14730. https://doi.org/10.1038/ncomms14730

Noël, B., van de Berg, W. J., Machguth, H., Lhermitte, S., Howat, I., Fettweis, X., & van den Broeke, M. R. (2016). A daily, 1 km resolution data set of downscaled Greenland ice sheet surface mass balance (1958–2015). *The Cryosphere*, *10*, 2361–2377. https://doi.org/10.5194/tc-10-2361-2016

Noh, M. J., & Howat, I. M. (2015). Automated stereo-photogrammetric DEM generation at high latitudes: Surface extraction with TIN-based search-space minimization (SETSM) validation and demonstration over glaciated regions. *GIScience and Remote Sensing*, *52*(2), 198–217. https://doi.org/10.1080/15481603.2015.1008621

Oerlemans, J., & Nick, F. M. (2005). A minimal model of a tidewater glacier. *Annals of Glaciology*, *42*, 1–6. https://doi.org/10.3189/172756405781813023

Paden, J., Li, J., Leuschen, C., Rodriguez-Morales, F., & Hale, R. (2010). *IceBridge MCoRDS L2 ice thickness, version 1. Boulder, Colorado USA*. NASA National Snow and Ice Data Center Distributed Active Archive Center. https://doi.org/10.5067/GDQ0CUCVTE2Q

Palmer, S., McMillan, M., & Morlighem, M. (2015). Subglacial lake drainage detected beneath the Greenland ice sheet. *Nature Communications*, *6*, 8408. https://doi.org/10.1038/ncomms9408

Palmer, S. J., Shepherd, A., Sundal, A., Rinne, E., & Nienow, P. (2010). InSAR observations of ice elevation and velocity fluctuations at the Flade Isblink ice cap, eastern North Greenland. *Journal of Geophysical Research*, *115*, F04037. https://doi.org/10.1029/2010JF001686

Pavlis, N. K., Holmes, S. A., Kenyon, S. C., & Factor, J. K. (2012). EGM2008: The development and evaluation of the Earth gravitational model 2008 (EGM2008). *Journal of Geophysical Research*, *117*(B4). https://doi.org/10.1029/2011JB008916

Pegler, S. S. (2018). Suppression of marine ice sheet instability. *Journal of Fluid Mechanics*, *857*, 648–680. https://doi.org/10.1017/jfm.2018.742

Pfeffer, W. T., Arendt, A. A., Bliss, A., Bolch, T., Cogley, J. G., Gardner, A. S., et al. (2014). The Randolph glacier inventory: A globally complete inventory of glaciers. *Journal of Glaciology*, *60*, 537–552. https://doi.org/10.3189/2014JoG13J176

Phillips, T., Rajaram, H., & Steffen, K. (2010). Cryo-hydrologic warming: A potential mechanism for rapid thermal response of ice sheets. *Geophysical Research Letters*, *37*, L20503. https://doi.org/10.1029/2010GL044397

Porter, C., Morin, P., Howat, I., Noh, M.-J., Bates, B., Peterman, K., et al. (2018). *ArcticDEM*. https://doi.org/10.7910/DVN/OHHUKH

Pritchard, H. D., Arthern, R. J., Vaughan, D. G., & Edwards, L. A. (2009). Extensive dynamic thinning on the margins of the Greenland and Antarctic ice sheets. *Nature*, *461*, 971–975. https://doi.org/10.1038/nature08471

Rahmstorf, S., Box, J., Feulner, G., Mann, M. E., Robinson, A., Rutherford, S., & Schaffernicht, E. J. (2015). Exceptional twentieth-century slowdown in Atlantic Ocean overturning circulation. *Nature Climate Change*, *5*, 475–480. https://doi.org/10.1038/nclimate2554

Rasmussen, L. (2004). Set fra oven: Et hjørne af Grønland. *Vejret*, *100*, 17–20.

Rastner, P., Bolch, T., Mölg, N., Machguth, H., Le Bris, R., & Paul, F. (2012). The first complete inventory of the local glaciers and ice caps on Greenland. *The Cryosphere*, *6*, 1483–1495. https://doi.org/10.5194/tc-6-1483-2012

Recinos, B., Maussion, F., Noël, B., Möller, M., & Marzeion, B. (2021). Calibration of a frontal ablation parameterisation applied to Greenland's peripheral calving glaciers. *Journal of Glaciology*, *67*, 1–1189. https://doi.org/10.1017/jog.2021.63

Rignot, E., Mouginot, J., & Scheuchl, B. (2011). Antarctic grounding line mapping from differential satellite radar interferometry. *Geophysical Research Letters*, *38*, L10504. https://doi.org/10.1029/2011GL047109

Rinne, E. J., Shepherd, A., Palmer, S., van den Broeke, M. R., Muir, A., Ettema, J., & Wingham, D. (2011). On the recent elevation changes at the Flade Isblink Ice Cap, northern Greenland. *Journal of Geophysical Research*, *116*, F03024. https://doi.org/10.1029/2011JF001972

Robel, A. (2017). Thinning sea ice weakens buttressing force of iceberg mélange and promotes calving. *Nature Communications*, *8*, 14596. https://doi.org/10.1038/ncomms14596

Sánchez-Gámez, P., Navarro, F. J., Benham, T. J., Glazovsky, A. F., Bassford, R. P., & Dowdeswell, J. A. (2019). Intra- and inter-annual variability in dynamic discharge from the Academy of Sciences Ice Cap, Severnaya Zemlya, Russian Arctic, and its role in modulating mass balance. *Journal of Glaciology*, *65*, 780–797. https://doi.org/10.1017/jog.2019.58

Scambos, T. A., Haran, T. M., Fahnestock, M. A., Painter, T. H., & Bohlander, J. (2007). MODIS-based Mosaic of Antarctica (MOA) data sets: Continent-wide surface morphology and snow grain size. *Remote Sensing of Environment*, *111*, 242–257. https://doi.org/10.1016/j.rse.2006.12.020

Schoof, C. (2007). Ice sheet grounding line dynamics: Steady states, stability, and hysteresis. *Journal of Geophysical Research*, *112*, F03S28. https://doi.org/10.1029/2006JF000664

Seehaus, T., Cook, A. J., Silva, A. B., & Braun, M. (2018). Changes in glacier dynamics in the northern Antarctic Peninsula since 1985. *The Cryosphere*, *12*, 577–594. https://doi.org/10.5194/tc-12-577-2018

Seehaus, T., Marinsek, S., Helm, V., Skvarca, P., & Braun, M. (2015). Changes in ice dynamics, elevation and mass discharge of Dinsmoor–Bombardier–Edgeworth glacier system, Antarctic Peninsula. *Earth and Planetary Science Letters*, *427*, 125–135. https://doi.org/10.1016/j.epsl.2015.06.047

Sergienko, O. V., & Wingham, D. J. (2021). Bed topography and marine ice-sheet stability. *Journal of Glaciology*, *68*(267), 124–138. https://doi.org/10.1017/jog.2021.79

Sevestre, H. (2015). *Surge-type glaciers: Controls, processes and distribution*. The University Centre in Svalbard.

Shepherd, A., Du, Z., Benham, T., Dowdeswell, J., & Morris, E. (2007). Mass balance of Devon ice cap, Canadian Arctic. *Annals of Glaciology*, *46*, 249–254. https://doi.org/10.3189/172756407782871279

Simonsen, S., Stenseng, L., Aðalgeirsdóttir, G., Fausto, R., Hvidberg, C., & Lucas-Picher, P. (2013). Assessing a multilayered dynamic firn-compaction model for Greenland with ASIRAS radar measurements. *Journal of Glaciology*, *59*(215), 545–558. https://doi.org/10.3189/2013JoG12J158

Strozzi, T., Luckman, A. J., Murray, T., Wegmuller, U., & Werner, C. L. (2002). Glacier motion estimation using SAR offset-tracking procedures. *IEEE Transactions on Geoscience and Remote Sensing*, *40*, 2384–2391. https://doi.org/10.1109/TGRS.2002.805079

Vaughan, D. G. (1995). Tidal flexure at ice shelf margins. *Journal of Geophysical Research: Solid Earth*, *100*(B4), 6213–6224. https://doi.org/10.1029/94JB02467

Vijay, S., & Braun, M. (2017). Seasonal and interannual variability of Columbia Glacier, Alaska (2011–2016): Ice velocity, mass flux, surface elevation and front position. *Remote Sensing*, *9*, 635. https://doi.org/10.3390/rs9060635

WCRP Global Sea Level Budget Group. (2018). Global sea-level budget 1993–present. *Earth System Science Data*, *10*, 1551–1590. https://doi.org/10.5194/essd-10-1551-2018

Wegmüller, U., Werner, C. L., Strozzi, T., Wiesmann, A., Frey, O., & Santoro, M. (2016). Sentinel-1 support in the GAMMA software. *Procedia Computer Science*, *100*, 1305–1312. https://doi.org/10.1016/j.procs.2016.09.246

Wendleder, A., Friedl, P., & Mayer, C. (2018). Impacts of climate and supraglacial lakes on the surface velocity of baltoro glacier from 1992 to 2017. *Remote Sensing*, *10*, 1681. https://doi.org/10.3390/rs10111681

Williamson, S., Sharp, M., Dowdeswell, J., & Benham, T. (2008). Iceberg calving rates from northern Ellesmere Island ice caps, Canadian Arctic, 1999–2003. *Journal of Glaciology*, *54*, 391–400. https://doi.org/10.3189/002214308785837048

Willis, M., Herried, B., Bevis, M., & Bell, R. E. (2015). Recharge of a subglacial lake by surface meltwater in northeast Greenland. *Nature*, *518*, 223–227. https://doi.org/10.1038/nature14116

Wood, M., Rignot, E., Fenty, I., An, L., Bjørk, A., van den Broeke, M., et al. (2021). Ocean forcing drives glacier retreat in Greenland. *Science Advances*, *7*(1), eaba7282. https://doi.org/10.1126/sciadv.aba7282

Zemp, M., Huss, M., Thibert, E., Eckert, N., McNabb, R., Huber, J., et al. (2019). Global glacier mass changes and their contributions to sea-level rise from 1961 to 2016. *Nature*, *568*, 382–386. https://doi.org/10.1038/s41586-019-1071-0